Aging and Disease
www.aginganddisease.org
Early access date: November 15, 2026
http://dx.doi.org/10.14336/AD.2026.1022

Original Article

Single-Cell Profiling Reveals an Aging-Enriched TLF^{+}CD209^{hi} Resident Macrophage State and Candidate Profibrotic Macrophage–Fibroblast Interactions in the Aging Heart

Youzhuo Quan[1, 2, 3#], Xiangyang Ma[1, 2, 3#], Liang Ren[4#], Zilong Liu[4], Zhengyan Wang[1, 2, 3], Xiaoxiao Han[5], Yi Song[5], Tianhui An[5], Zhaohui Wang[5], Kun Liu[1, 2, 3*], Cheng Fan[5*]

[1]Department of Cardiology, Union Hospital, Tongji Medical College, Huazhong University of Science and Technology, Wuhan, China; [2]Hubei Key Laboratory of Biological Targeted Therapy, Union Hospital, Tongji Medical College, Huazhong University of Science and Technology, Wuhan, China; [3]Hubei Engineering Research Center for Immunological Diagnosis and Therapy of Cardiovascular Diseases, Union Hospital, Tongji Medical College, Huazhong University of Science and Technology, Wuhan, China; [4]Department of Forensic Medicine, Tongji Medical College, Huazhong University of Science and Technology, Wuhan, China; [5]Department of Geriatrics, Union Hospital, Tongji Medical College, Huazhong University of Science and Technology, Wuhan, China

[Received August 10, 2026; Revised November 9, 2026; Accepted November 10, 2026]

ABSTRACT: Cardiac aging is characterized by diastolic dysfunction, interstitial fibrosis, and increased risk of heart failure with preserved ejection fraction (HFpEF), yet how macrophage heterogeneity, senescence, and intercellular signaling converge during physiological aging remains unclear. We integrated echocardiography, histology, immunostaining, flow cytometry, and single-cell RNA sequencing of sorted CD45^{+} cells from young and aged C57BL/6J mouse hearts, alongside human cardiac immunostaining. Aged mice developed diastolic dysfunction, ventricular remodeling, cardiomyocyte hypertrophy, and interstitial fibrosis, accompanied by immune-cell expansion. Exploratory single-cell transcriptomic analysis of pooled young and aged cardiac immune-cell libraries highlighted macrophages as a prominently remodeled immune population and identified an aging-enriched TLF^{+} (expressing *Timd4* and/or *Lyve1* and/or *Folr2*) CD209^{hi} state within the tissue-resident macrophage compartment. Aged macrophages displayed increased senescence-associated secretory phenotype-related transcriptional activity, pro-inflammatory and profibrotic programs, and subset-specific metabolic and regulatory transcriptional programs. MHC-II^{+} macrophages showed a glycolytic inflammatory state, whereas TLF^{+}CD209^{hi} macrophages exhibited profibrotic programs enriched for extracellular matrix remodeling, epidermal growth factor family signaling, and IL-10-associated communication. Cell–cell communication and flow cytometry nominated HB-EGF/AREG–EGFR and IL-10-associated PDGF-A/PDGFRα signaling as candidate macrophage–fibroblast profibrotic circuits. In primary adult mouse cardiac fibroblasts, HB-EGF and PDGF-AA increased selected fibrosis-associated markers and EGFR/ERK or PDGFRα/ERK phosphorylation, respectively; pharmacological inhibition attenuated some responses. These findings link macrophage senescence-associated remodeling and an aging-enriched TLF^{+}CD209^{hi} state to fibrosis-associated features and nominate EGF-family ligands and IL-10-associated PDGF-A/PDGFRα signaling as candidate contributors to fibroblast activation and myocardial fibrosis during physiological cardiac aging. However, their causal roles in vivo remain to be established by targeted genetic or pharmacologic perturbation.

Keywords: Cardiac aging, Macrophages, Myocardial fibrosis, SASP, Single-cell RNA sequencing

***Correspondence should be addressed to:** Dr. Cheng Fan (Email: kristyfan@hust.edu.cn) and Dr. Kun Liu (Email: liukun@hust.edu.cn), Union Hospital, Tongji Medical College, Huazhong University of Science and Technology, Wuhan 430022, China. [#] The authors contributed equally to this work.

Copyright: © 2026 Quan Y. et al. This is an open-access article distributed under the terms of the Creative Commons Attribution License, which permits unrestricted use, distribution, and reproduction in any medium, provided the original author and source are credited.

INTRODUCTION

Aging drives progressive changes in cardiac structure and function that predispose to heart failure with preserved ejection fraction (HFpEF), characterized predominantly by diastolic dysfunction and interstitial fibrosis [1]. While cardiomyocyte alterations contribute substantially to age-related remodeling, increasing evidence implicates immune cells — and macrophages in particular — as active modulators of myocardial homeostasis and fibrosis during aging and after injury [2, 3]. Macrophage expansion and phenotypic shifts have been linked to adverse remodeling and impaired relaxation [4], supporting immune remodeling as an important component of cardiac aging.

Recent single-cell and fate-mapping studies have revealed substantial heterogeneity among cardiac macrophages, distinguishing long-lived tissue-resident populations (marked by TIMD4, LYVE1, and FOLR2) from recruited $CCR2^{+}$/$MHC\text{-}II^{+}$ subsets with distinct ontogeny and functions [5, 6]. These resident subsets play important roles in tissue surveillance, homeostasis and repair, but their behavior during physiological aging — including whether aging-enriched populations emerge and how they communicate with fibroblasts — remains unclear.

Cellular senescence and the accompanying senescence-associated secretory phenotype (SASP) drive chronic low-grade inflammation and tissue dysfunction in multiple organs; macrophages with senescence-associated features are increasingly recognized as contributors to inflammaging and fibrotic disease [7, 8]. In parallel, metabolic reprogramming (a shift between FAO/OXPHOS and glycolysis) underlies macrophage polarization and effector functions, linking cellular metabolism to pro-inflammatory versus pro-repair phenotypes [9]. How senescence, metabolism and subset-specific regulatory programs converge in cardiac macrophages during age-related fibrotic remodeling has not been fully elucidated.

Here, using integrated echocardiographic, histologic, flow cytometric and single-cell transcriptomic analyses, combined with regulatory network and cell–cell communication inference, we define age-associated macrophage remodeling and identify an aging-enriched $TLF^{+}CD209^{hi}$ tissue-resident macrophage state linked to fibroblast-interacting EGF-family and IL-10-associated PDGF-A/PDGFRα signaling. Functional experiments further showed that recombinant HB-EGF and PDGF-AA activated cardiac fibroblasts through EGFR/ERK and PDGFRα/ERK signaling, respectively, providing functional support for the candidate pathways nominated by the single-cell analyses.

METHODS

Human samples

Full-thickness human left ventricular free-wall myocardium was collected at autopsy from the Department of Forensic Medicine, Tongji Medical College, Huazhong University of Science and Technology. Twenty donors were included: ten young individuals (<45 years) and ten older individuals (>65 years). All donors died of non-cardiac causes and had no clinical history or autopsy evidence of primary cardiac disease (ischemic heart disease, cardiomyopathy, myocarditis, or major structural abnormalities). Cases with prolonged agonal events, systemic sepsis, or post-mortem intervals >24 hours were excluded. Autopsies followed institutional protocols; written informed consent for autopsy and research use of tissue was obtained from next of kin. The study was approved by the Ethics Committee of Tongji Medical College, Huazhong University of Science and Technology (NO.: IROG20250841) and complied with the Declaration of Helsinki and local regulations for post-mortem research.

At autopsy, ~0.5–1.0 cm^3 full-thickness samples were excised from the mid-level left ventricular free wall using sterile, RNase-/DNase-free instruments. To minimize regional variability, all samples were taken from the same anatomical location. Specimens were rinsed in ice-cold PBS to remove blood, fixed in 10% neutral-buffered formalin for 24–48 h at room temperature, processed through graded ethanol, cleared in xylene, and embedded in paraffin using standard histopathological workflows. All staining was performed in batch-matched conditions to reduce technical variation between young and elderly donor samples.

Animals

Male C57BL/6J mice were used: young (8–10 weeks) and aged mice (18–22 months). Mice were obtained from Hubei Provincial Laboratory Animal Public Service Center and maintained in filter-top cages under specific-pathogen-free conditions, with ad libitum access to standard chow and water, a 12 h light/12 h dark cycle, and controlled temperature and humidity. All experimental procedures were reviewed and approved by the Institutional Animal Care and Use Committee of Tongji Medical College, Huazhong University of Science and Technology (No.20240305684). All procedures conformed to the guidelines from Directive 2010/63/EU of the European Parliament on the protection of animals used for scientific purposes and the National Institutes of Health Guide for the Care and Use of Laboratory Animals. Mice were anesthetized appropriately for all procedures

and every effort was made to minimize suffering. At the conclusion of all procedures, mice were euthanized humanely. Euthanasia was performed by CO_2 asphyxiation using a gradual fill method followed by cervical dislocation to ensure death. CO_2 was administered at a flow rate sufficient to displace 30%–70% of the chamber volume per minute. Death was confirmed by the absence of respiration and cardiac activity before tissue collection.

Echocardiography

Mice were anesthetized with isoflurane delivered in 100% oxygen via a nose cone. Anesthesia was induced with 3.5% isoflurane and maintained with 1.8–2.0% isoflurane. Oxygen was delivered at 1.0 L/min to achieve and maintain stable anesthesia during transthoracic echocardiography, with respiratory and heart rates monitored throughout. The left ventricular function was assessed by transthoracic echocardiography using a VisualSonics Vevo LAZR-X Imaging System (Visual Sonics, Toronto, Canada) with a 40-MHz MicroScan transducer (model MS-550D) [10]. Both systolic and diastolic functions were analyzed. Left ventricular internal diameter in diastole (LVIDd) and systole (LVIDs), heart rate (HR), left ventricular posterior wall thickness in diastole (LVPWd) and systole (LVPWs) were measured on the M-mode tracings and were averaged from 5 cardiac cycles. Left ventricular ejection fraction (% LVEF), left ventricular fractional shortening (% LVFS), E/e' and E/A were calculated.

Histological analysis

Hearts were fixed in 4% paraformaldehyde for 24 h, embedded in paraffin and sectioned at 5 μm. Masson's trichrome (Servicebio) and wheat germ agglutinin (WGA; Thermo Fisher) staining were performed per manufacturers' protocols to evaluate interstitial fibrosis and cardiomyocyte size, respectively. For immunohistochemistry, sections were incubated with primary anti-CD45 antibodies (Abcam, ab208022, 1:500) followed by a biotinylated secondary antibody and avidin–biotin enzyme complex (Vectastain kit, Vector Laboratories). For immunofluorescence, sections were permeabilized with 0.1% Triton X-100 in PBS and blocked in 4% bovine serum albumin (BSA) in PBS for 1 h at room temperature. Primary antibodies were applied overnight at 4 °C; after washing, sections were incubated with appropriate fluorescent secondary antibodies and DAPI (SouthernBiotech) for 1 h at room temperature in the dark. The primary antibodies were anti-Human CD68 (Abcam, ab303565, 1:4000), anti-Mouse F4/80 (CST, 70076, 1:500), anti-Human/Mouse Lyve1 (Thermo Fisher Scientific, 53-0443-82, 1:100), anti-Human CD209 (Novus, NBP2-53275, 1:200), anti-Mouse CD209 (PTG, 84365-5-RR, 1:200), anti-Human cTnT (PTG, 15513-1-AP, 1:200), anti-Mouse cTnT (PTG, 15513-1-AP, 1:200) antibodies. The secondary antibodies were goat anti-rabbit IgG (Abcam, ab205718), goat anti-mouse IgG (Abcam, ab205719), iFluor® 647 tyramide (aatbio, 11066), iFluor® 555 tyramide (aatbio, 11065) and iFluor® 488 tyramide (aatbio, 11060). Images were captured using an Olympus IX73 microscope (DP73 camera) or a Zeiss confocal microscope and analyzed with Image-Pro Plus software.

For quantitative histological analyses, two sections per heart were analyzed, with five randomly selected microscopic fields quantified per section. For Masson's trichrome staining, fibrosis was quantified as the percentage of collagen-positive area relative to the total myocardial tissue area within each field. Measurements from all quantified fields were averaged to generate a single value for each heart.

For the representative immunofluorescence analyses shown in Figure 3E–F, two sections per heart were examined, with multiple microscopic fields evaluated in each section. Representative images were selected to illustrate the observed staining patterns.

Representative histological, immunofluorescence, flow cytometry, and immunoblot images were selected to reflect the typical findings observed across experimental samples within each group, rather than the most pronounced or extreme examples.

For immunofluorescence staining of primary mouse cardiac fibroblasts grown on coverslips, cells were fixed with 4% paraformaldehyde for 15 min at room temperature, permeabilized with 0.1% Triton X-100 in PBS for 10 min, and blocked with 4% BSA in PBS for 1 h. Cells were then incubated overnight at 4 °C with primary antibodies against α-SMA (Abcam, ab124964, 1:200) and vimentin (Boster, BM0135, 1:100). After washing with PBS, cells were incubated with appropriate fluorescent secondary antibodies and DAPI for 1 h at room temperature in the dark. Coverslips were mounted with antifade mounting medium, imaged using a Zeiss confocal microscope or an Olympus IX73 microscope.

Flow cytometry

Mouse hearts were perfused retrogradely with ice-cold PBS containing 1% fetal bovine serum (FBS). Hearts were dissected, minced, and enzymatically digested in Hanks' Balanced Salt Solution (HBSS; Sigma-Aldrich, H9269) with 1 mg/mL collagenase type II (Merck, 1148090), 100 U/mL hyaluronidase (Sigma-Aldrich, H4272), and 100 U/mL DNase I (Sigma-Aldrich, 69182) [11]. Samples were agitated and incubated on a shaker for

30 min at 37 °C. Digests were triturated, filtered through a 40 μm mesh, and centrifuged at 1680 rpm for 10 min at 4 °C. Red blood cells were lysed (Invitrogen, 00-4333-57), and cells were washed in HBSS with 2% FBS and 0.2% BSA. Antibody staining was performed on ~1×10^6 cells in 100 μL for 30–45 min on ice in the dark. Antibodies included anti-CD45 (BioLegend, 557659), anti-CD11b (BD Pharmingen, 5579609), anti-F4/80 (BioLegend, 123137), anti-LYVE1 (Invitrogen, 53-0443-82), anti-Tim-4 (BioLegend, 130007), anti-FOLR2 (Novus, NBP2-81079AF647), anti-MHC-II (BioLegend, 107629), Anti-CD209a (BioLegend, 833003), anti-IL-6 (BioLegend, 504507), anti-TNF-α (BioLegend, 506307), anti-IL-10 (BioLegend, 505031), anti-IL-1β (Invitrogen, 17-7114-80), anti-HB-EGF (Santa Cruz, sc-365182 AF647), anti-Amphiregulin (Santa Cruz, sc-74501 AF647), anti-PDGF-A (Santa Cruz, sc-9974 AF647). In the single-cell transcriptomic analysis, TLF refers to resident macrophages expressing one or more of these markers (*Timd4* and/or *Lyve1* and/or *Folr2*), consistent with the established definition [6]. For flow-cytometric phenotyping, surface LYVE1 positivity was used as an operational marker to identify the corresponding resident macrophage compartment. Thus, the flow-cytometric TLF gate was based on LYVE1 expression rather than simultaneous protein-level detection of all three TLF markers. Appropriate fluorescence-minus-one (FMO) controls and single-stain compensation controls were included for panel design. The CD209-positive gate was defined using the CD209 FMO control (Supplementary Fig. 15) and applied unchanged to all young and aged samples; cells above and below this threshold were designated as TLF^+CD209^{hi} and TLF^+CD209^{lo}, respectively. Data were acquired on a BD FACSVerse and analyzed using FlowJo.

For absolute cell quantification, cardiac tissue was weighed before digestion. The total number of viable cells recovered after digestion was recorded, and absolute macrophage-subset numbers were calculated from the corresponding flow-cytometric frequencies and normalized to tissue weight, expressed as cells per mg heart tissue.

Isolation of primary adult mouse cardiac fibroblasts

Primary adult mouse cardiac fibroblasts were isolated as previously described with minor modification [12]. Briefly, mouse hearts were excised, rinsed with cold sterile PBS, and minced into approximately 2-mm pieces. The minced heart tissues were incubated in D-Hanks' balanced salt solution containing 0.05% EDTA-free trypsin on ice with gentle shaking for 30 min. Thereafter, the tissue fragments were digested with collagenase II (1 mg/mL) in D-Hanks' balanced salt solution at 37 °C with gentle rotation. During digestion, the tissues were gently triturated every 5 min for a total of five cycles. Digestion was terminated with high-glucose DMEM supplemented with 10% FBS. The resulting cell suspension was filtered through a 40-μm cell strainer and centrifuged at 300 × g for 10 min. Cells were resuspended in complete high-glucose DMEM containing 10% FBS and seeded onto culture dishes. After two hours, non-adherent cells were removed, and the adherent cardiac fibroblasts were maintained in 10% FBS high glucose DMEM complete medium.

For stimulation experiments, primary mouse cardiac fibroblasts were serum-starved overnight and then treated with recombinant HB-EGF (MCE, HY-P7194; 100 ng/mL) or PDGF-AA (MCE, HY-P7277; 100 ng/mL). Where indicated, cells were pretreated with the EGFR inhibitor AG1478 (MCE, HY-13524; 2 μM) or the PDGFR inhibitor imatinib (MCE, HY-15463; 1 μM) for 60 min before stimulation with HB-EGF or PDGF-AA, respectively. The inhibitors remained in the culture medium throughout ligand stimulation. Cells were stimulated for 15 min to assess EGFR, PDGFRα, and ERK1/2 phosphorylation, for 24 h to evaluate *Acta2*, *Col1a1*, and *Col3a1* mRNA expression by RT-qPCR, and for 48 h to assess COL1A1, COL3A1, and α-SMA protein expression by Western blotting and α-SMA organization by immunofluorescence. Vehicle-treated cells served as controls.

For the experiments presented in Figure 7, primary cardiac fibroblasts were independently isolated from four young adult mice per treatment group (n = 4 biological replicates per group), with each mouse contributing one independent fibroblast culture. Different treatment groups used fibroblasts from distinct donor mice, without sharing or pooling fibroblast isolations. Therefore, the treatment groups were independent and no pairing was involved.

Western blotting

Total protein was extracted from cells using RIPA lysis buffer supplemented with protease and phosphatase inhibitor cocktails. Protein concentrations were measured with a BCA protein assay kit. Equal amounts of protein were resolved by SDS-PAGE and electrotransferred onto PVDF membranes. After blocking with protein free rapid blocking buffer, the membranes were incubated with the indicated primary antibodies overnight at 4 °C. Membranes were then washed and incubated with secondary antibodies at room temperature for two hours. Immunoreactive bands were detected using an enhanced chemiluminescence substrate and quantified with ImageJ software. Phosphorylated protein levels were normalized to their corresponding total protein levels, whereas COL1A1, COL3A1, and α-SMA levels were normalized

to GAPDH. The resulting values were expressed relative to the vehicle-treated control group, which was set to 1. The primary antibodies used for Western blotting are as follows: GAPDH (Selleck, F0003), α-SMA (Selleck, F0017), COL1A1 (Selleck, F1228), COL3A1 (Absin, abs118863), p-ERK1/2 (Selleck, F0007), ERK1/2 (Selleck, F0002), p-EGFR (Selleck, F0298), EGFR (Proteintech, 30847-1-AP), p-PDGFRα (Thermo Fisher Scientific, PA5-17070), PDGFRα (Selleck, F3240).

Real-time quantitative PCR (RT-qPCR)

Total RNA was extracted using TRIzol reagent according to the manufacturer's instructions and reverse-transcribed into cDNA using HiScript III RT SuperMix. RT-qPCR was performed using AceQ qPCR SYBR Green Master Mix on a CFX96 Real-Time PCR Detection System. Each reaction was performed in duplicate or triplicate. Relative gene expression was normalized to GAPDH and calculated using the $2^{-\Delta\Delta CT}$ method, with the vehicle-treated control group used as the calibrator (set to 1). The mouse primer sequences used for RT-qPCR are listed in Supplementary Table 6.

Cell preparation and sorting

Hearts were processed as above. $CD45^+$ cells were enriched and sorted on a Beckman Coulter cell sorter. Cell counts and viability were measured using a Countstar® Rigel S2 automated cell analyzer with AO/PI staining. Following optional debris and dead-cell removal (Miltenyi kits), fresh cells were washed twice in RPMI-1640, resuspended at 1×10^6 cells/mL in 1× PBS with 0.04% BSA, and processed immediately for single-cell capture.

Single-cell RNA-seq library construction and sequencing

For single-cell RNA sequencing, hearts from four young mice were pooled to generate the young library, whereas hearts from two aged mice were pooled to generate the aged library. The larger number of young hearts was required because individual young hearts yielded fewer viable cells after tissue dissociation, and pooling four hearts was necessary to obtain sufficient cell input for single-cell capture and library preparation. Thus, one pooled scRNA-seq library was generated for each age group. Single-cell 3′ libraries were prepared using the SeekOne® Digital Droplet Single Cell 3′ library preparation kit (SeekGene, Catalog No. K00202) according to the manufacturer's instructions [13]. In brief, cells were combined with reverse transcription reagents and loaded into SeekOne® DD Chip S3; barcoded hydrogel beads and partitioning oil were added to generate emulsion droplets. Reverse transcription was performed at 42 °C for 90 min and inactivated at 80 °C for 5 min. Emulsions were broken, cDNA purified and amplified by PCR; amplified cDNA was fragmented, end-repaired, A-tailed, ligated to adapters and indexed by PCR to capture the 3′ polyadenylated fragments with cell barcode and UMI. Libraries were cleaned with SPRI beads, quantified by qPCR (KAPA Biosystems KK4824), and sequenced on an Illumina NovaSeq 6000 (PE150).

All mice contributing to the scRNA-seq libraries were male. Young and aged samples were processed in the same experimental batch using the same SeekOne® Digital Droplet Single Cell 3′ library preparation workflow, and both libraries were sequenced on the same Illumina NovaSeq 6000 platform.

Sequencing data quality control

Raw reads were trimmed and filtered with fastp (v0.20.1) [14] to remove primer/adaptor sequences and low-quality bases and to collect basic quality statistics. Parameters included: a 1-bp sliding window from the 3′ end with base trimming when mean quality <3; auto-adapter detection for paired-end data; removal of reads shorter than 60 bp after trimming.

Read processing and gene-barcode matrix generation

Cleaned reads were processed with the SeekSoul Tools pipeline (v 1.0.0) to generate gene × barcode UMI count matrices [13]. Briefly, cell barcodes and UMI sequences were extracted according to the kit's read structure and corrected against a whitelist. Reads were aligned to the reference genome (refdata-gex-mm10-2020-A) using STAR (v2.5.1b), and reads were assigned to transcripts using featureCounts (Subread package) [15]. A raw UMI count matrix (analogous to Cell Ranger's raw_feature_bc_matrix) was generated. Cell calling was performed using a two-step algorithm conceptually similar to Cell Ranger/EmptyDrops [16]: (1) identification of high-RNA barcodes by total UMI cutoff to capture high-content cells, and (2) profile-based testing of remaining barcodes to distinguish low-RNA cells from empty partitions, yielding a filtered_feature_bc_matrix.

Single-cell transcriptomic data processing and analysis

Downstream analyses were performed in Seurat (v5.5.0) [17]. Low-quality cells were first filtered out based on standard quality control metrics: nFeature_RNA between 600 and 4000, nCount_RNA between 1000 and 30000, and percent.mt < 8%. Doublets were subsequently

identified using scDblFinder (v1.24.10) [18], with sample identity (orig.ident) specified for sample-aware doublet detection. Cells classified as doublets were excluded from all downstream analyses. In total, 2,272 of 21,463 cells (10.6%) were identified as doublets and removed, leaving 19,191 singlets for downstream analysis. Subsequently, to enrich for immune cells, cells with *Ptprc* expression >0.125 were retained. This operational cutoff was selected based on the empirical distribution of *Ptprc* expression. The expression distribution and sensitivity of cell retention to alternative *Ptprc* thresholds are presented in Supplementary Figure 18 and Supplementary Table 5, respectively. Ambient RNA contamination was subsequently assessed using decontX (v1.6.0) [19], and cells with high estimated contamination were excluded. To obtain an integrated view of the cardiac immune landscape, cells from all samples were merged, normalized, and scaled. The top 2,000 highly variable genes were selected for principal component analysis (PCA). To correct for technical batch effects, we performed data integration using Harmony (v2.0.5) [20] on the top 30 principal components (PCs). A shared nearest neighbor (SNN) graph was constructed based on the Harmony-corrected space (using PCs 1–30), and cells were clustered using the Louvain algorithm (resolution =1). The results were visualized using Uniform Manifold Approximation and Projection (UMAP). Major cell lineages were annotated based on canonical marker genes. For higher-resolution analysis of macrophage heterogeneity, macrophages identified in the global immune-cell atlas were subset from the Seurat object and independently reprocessed. The macrophage subset was re-normalized, highly variable features were re-identified, the data were rescaled, and a new macrophage-specific PCA was calculated. CCA-based integration was then performed using this newly generated macrophage-specific PCA space and was not applied to the Harmony-corrected embedding generated during the global immune-cell analysis. The first 30 dimensions of the resulting CCA-integrated reduction were used for SNN graph construction, clustering, and UMAP visualization.

Differential expression analysis

Differentially expressed genes (DEGs) between groups were identified using the FindMarkers function in Seurat with the MAST (v1.36.0) [21] test. *P* values were adjusted for multiple testing using the Bonferroni correction. Genes with an absolute $|\log_2 FC| \geq 0.5$, min.pct > 0.1, and adjusted $P < 0.05$ were considered differentially expressed. Because the scRNA-seq dataset comprised one pooled library per age group, these differential-expression analyses were performed at the cell level for exploratory purposes and were not interpreted as biological replicate-level statistical inference.

Age-associated transcriptional remodeling score

To descriptively compare the magnitude of age-associated transcriptional changes across immune-cell subsets, we calculated an FCscore as described previously [22]. Briefly, for each subset, the top 100 genes upregulated in aged versus young cells were identified and used to derive the FCscore according to the published method. The FCscore was used solely as a descriptive measure of the relative magnitude of age-associated transcriptional remodeling across immune populations and was not interpreted as a measure of functional or causal contribution to cardiac aging or tissue pathology.

Pseudotime and transcriptional module analysis

Macrophage state transitions were reconstructed using Slingshot (v2.14.0) [23]. Differential pseudotime distributions were compared with Kolmogorov–Smirnov tests. Genes with condition-dependent expression along pseudotime were identified using tradeSeq (v1.20.0) [24] with a negative binomial GAM (fitGAM, nknots = 6) and conditionTest. Genes with condition-dependent patterns were clustered by smoothed expression using K-means in ClusterGVis (v0.1.1) into four modules; each module underwent Gene Ontology (GO) and Kyoto Encyclopedia of Genes and Genomes (KEGG) enrichment analysis and was visualized with visCluster.

Regulon and transcription factor (TF) activity analysis (SCENIC)

Regulatory network analysis was performed using SCENIC (v1.3.2). Regulon activity (AUC) matrices and regulon lists were loaded from preprocessed loom outputs and analyzed with SCopeLoomR and SCENIC/pySCENIC tools. Regulon specificity scores (RSS) were calculated to identify cell-type–specific regulon activation.

Metabolic pathway activity analysis

Metabolic pathway activity per subset was quantified using a published pathway-scoring algorithm [25]. KEGG pathway scores were calculated as weighted mean expression of pathway member genes (weights inverse to gene pathway promiscuity). Statistical significance was assessed by permutation testing (5,000 shuffles; $P < 0.01$).

Cell-cell communication analysis

Because CD45 immunomagnetic enrichment does not

completely deplete non-immune cells, residual CD45-low/negative stromal and vascular cells were present in the raw count matrix. Therefore, we reprocessed the raw counts without the Ptprc_RNA > 0.125 filter used for primary immune-cell clustering (Section 2.13) to retain residual fibroblast and endothelial clusters for CellChat analysis. The reprocessed dataset used the same preprocessing/integration as Section 2.13 and showed high concordance with the original immune clusters (Supplementary Fig.10). Cluster identities were then used to infer intercellular communication with CellChat (v1.6.1) [26]. Separate CellChat objects were created for aged and young samples using normalized expression and cluster identities. The CellChat mouse ligand-receptor database (CellChatDB.mouse) was used. Communication probabilities were computed with computeCommunProb and aggregated at the pathway level (computeCommunProbPathway). Differential network analysis identified differentially enriched signaling pathways between age groups. Unless otherwise indicated, signaling pathway activity and ligand–receptor interactions were inferred from transcriptomic data.

Correlation analysis

For cells co-expressing both target genes (expression > 0), Spearman's rank correlation analysis was performed using the cor.test function in R. The Spearman correlation coefficient (ρ) and corresponding *P* value are reported and displayed in the associated scatter plots.

Statistical analysis

For datasets with n ≥ 6 per group, data distribution was assessed using the Shapiro–Wilk test. Normally distributed data were analyzed using parametric tests, whereas non-normally distributed data were analyzed using non-parametric tests. For all datasets with n < 6 per group, non-parametric tests were used irrespective of the apparent data distribution. Comparisons between two independent groups were performed using the two-tailed unpaired Student's t-test when n ≥ 6 and the data were normally distributed; otherwise, the two-tailed Mann–Whitney U test was used. For comparisons among three groups, all of which involved n = 4 per group in the present study, the Kruskal–Wallis test followed by Dunn's multiple-comparisons test was used, with adjustment for two prespecified pairwise comparisons per analysis. The exact statistical test used for each analysis is specified in the corresponding figure legend. A two-tailed $P < 0.05$ was considered statistically significant.

For animal experiments, the individual mouse was considered the biological and statistical unit; measurements obtained from multiple fields or technical measurements within the same animal were averaged before statistical analysis. For human histological analyses, each individual donor was considered one biological replicate. For in vitro fibroblast experiments, each independent biological experiment was considered one replicate. For scRNA-seq analyses, individual cells were used as observational units for exploratory cell-level comparisons; however, because one pooled library was generated per age group, cells were not considered independent biological replicates, and cell-level statistical tests were not interpreted as biological replicate-level inference.

RESULTS

Aging hearts exhibit diastolic dysfunction and structural remodeling accompanied by immune cell accumulation

To define the baseline cardiac phenotype associated with physiological aging, we performed transthoracic echocardiography and histological analyses in young and aged mice and examined post-mortem human heart samples from young and older donors. Representative M-mode, pulse-wave Doppler (PWD), and tissue Doppler imaging (TDI) tracings demonstrated clear age-dependent alterations in cardiac function (Figure 1A-J). Systolic performance was largely preserved, as aged mice exhibited only a modest reduction in LVEF (Fig. 1B) with no significant change in LVFS (Fig. 1C). In contrast, diastolic indices were markedly impaired: the E/e′ ratio was significantly increased, whereas the E/A ratio was significantly decreased in aged animals, consistent with impaired ventricular relaxation and elevated filling pressures (Fig. 1D–E). These functional changes were accompanied by structural remodeling. Aged mice displayed enlarged LVIDd and LVIDs (Fig. 1F–G), while LVPWd and LVPWs remained comparable between age groups (Fig. 1H–I). HR was slightly decreased in aged mice (Fig. 1J).

Histological analyses further confirmed age-associated remodeling. Compared with young controls, aged mouse hearts exhibited increased cardiomyocyte cross-sectional area, indicative of hypertrophy, and significantly greater interstitial collagen deposition (Fig. 1K, L, N). Notably, immunostaining for CD45 revealed a marked expansion of cardiac immune cells in aged hearts (Fig. 1K, P), indicating enhanced immune cell accumulation with aging. Human cardiac tissues from older donors recapitulated these structural features, showing increased cardiomyocyte size, more extensive fibrosis, and higher densities of $CD45^+$ immune cells compared with young individuals (Fig. 1K, M–Q). The parallel increase in cardiac immune cells across species

provided the rationale for subsequent single-cell profiling of CD45⁺ populations to identify immune subsets involved in age-associated myocardial remodeling and inflammation.

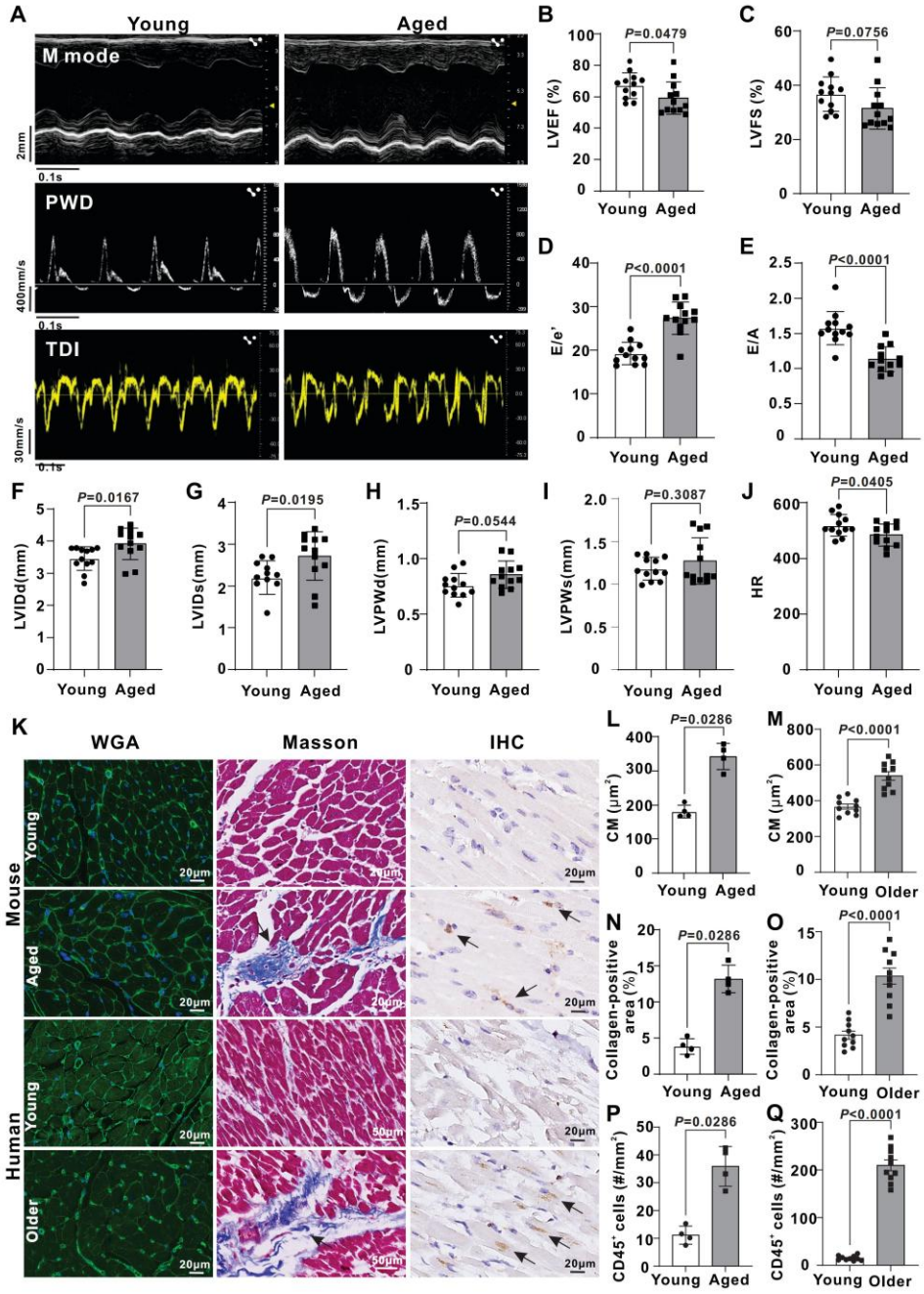


Figure 1. Aging induces diastolic dysfunction, structural remodeling, and immune cell accumulation in the heart. (A) Representative transthoracic echocardiographic images from young and aged mice, including M-mode, PWD, and TDI. **(B–J)** Quantitative analyses of cardiac structure and function: LVEF **(B)**, LVFS **(C)**, E/e′ ratio **(D)**, E/A ratio **(E)**, LVIDd **(F)** and LVIDs **(G)**, LVPWd **(H)** and LVPWs **(I)**, and HR **(J)**. **(K)** Representative histological images of cardiac sections from young and aged mice and humans showing wheat germ agglutinin (WGA) staining for cardiomyocyte cross-sectional area, Masson's trichrome staining for interstitial collagen (blue), and CD45 immunohistochemistry indicating immune cell infiltration. **(L–Q)** Quantification of cardiomyocyte (CM) cross-sectional area **(L, M)**, fibrotic area **(N, O)**, and CD45⁺ cell density **(P, Q)** in mouse **(L, N, P)** and human **(M, O, Q)** hearts from young and aged groups. Scale bars, as indicated. Mouse studies: n = 12 mice per group for echocardiography and n = 4 mice per group for histology. Human studies: n = 10 donors per group. Data in Figure 1L, 1N, and 1P are presented as median with interquartile range and were analyzed using the two-tailed Mann–Whitney U test. All other quantitative data are presented as mean ± SEM and were analyzed using the unpaired two-tailed Student's t-test. Exact *P* values are shown in the corresponding panels.

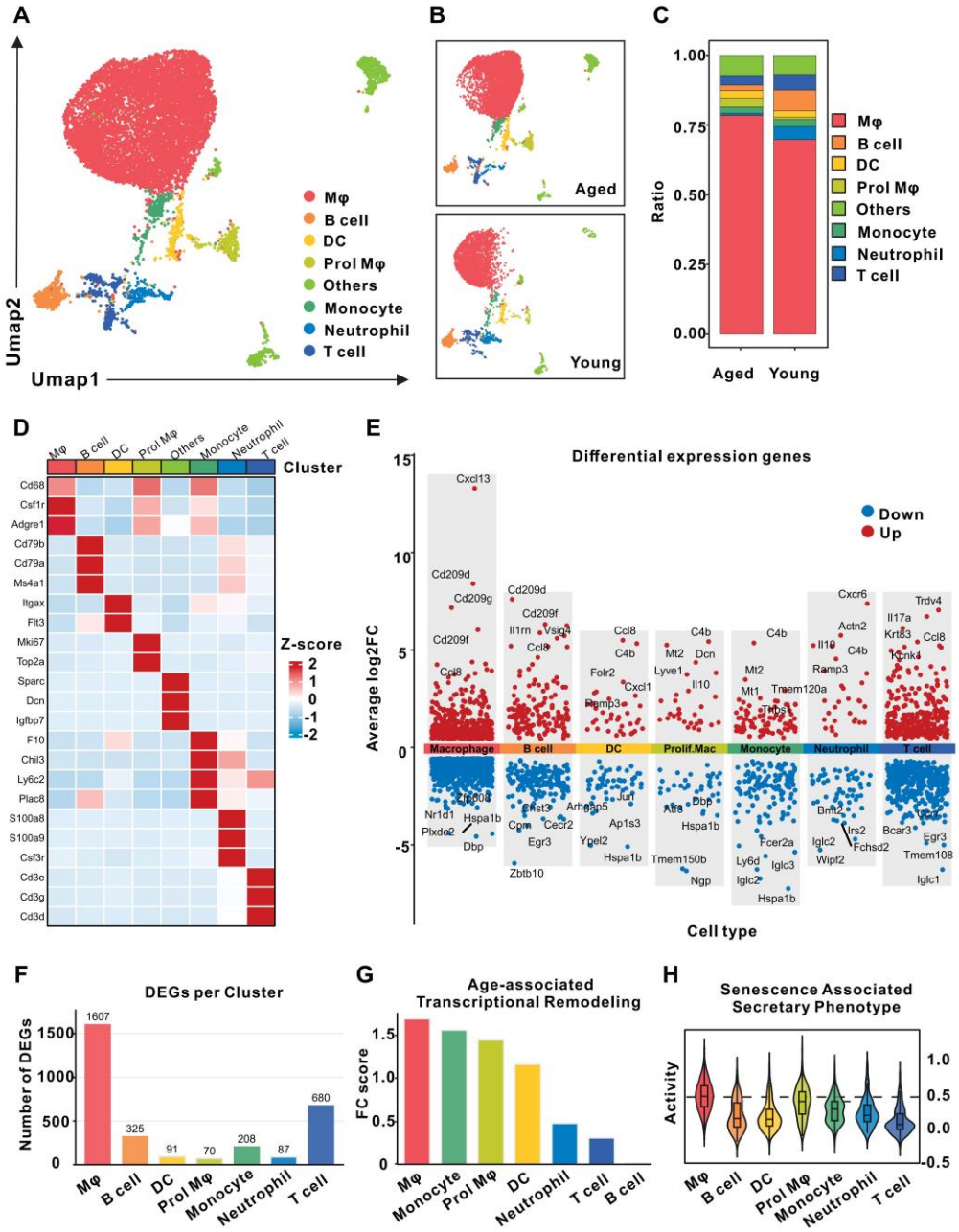


Figure 2. Exploratory single-cell profiling highlights prominent age-associated transcriptional remodeling in cardiac macrophages. (A) UMAP visualization of all cardiac CD45⁺ cells from young and aged mouse hearts after unsupervised clustering, revealing eight major immune populations. Each dot represents a single cell. **(B)** The same UMAP space as in **(A)**, split by age group, to show the spatial distribution of young and aged cardiac CD45⁺ cells. **(C)** Bar plots showing proportional frequencies of each immune cell population in the pooled young and aged scRNA-seq libraries. **(D)** Heatmap of row Z-score–normalized expression of representative marker genes defining each immune cluster. **(E)** Differential gene expression analysis showing up- and down-regulated genes across different immune-cell types between aged and young hearts. DEGs were identified using MAST as implemented in Seurat ($|\log_2 FC| \geq 0.5$, min.pct > 0.1, adjusted $P < 0.05$). Upregulated and downregulated genes are indicated in red and blue, respectively. **(F)** Bar plots quantifying the total number of significantly up- and down-regulated genes combined within each immune cluster, as identified in **(E)**. **(G)** Contribution analysis quantifying the relative contribution of each immune population to age-associated transcriptional remodeling. Higher scores indicate greater transcriptional remodeling. Scores were calculated from the top 100 age-regulated genes. **(H)** Violin plots with embedded box plots showing SASP pathway activity scores calculated using AddModuleScore for each immune cell subset in aged hearts. Box plots indicate median, interquartile range, and 1.5× interquartile range (whiskers). Single-cell transcriptomic analyses presented in Figures 2–6 were exploratory and based on one pooled library per age group (four young mice and two aged mice per library); individual cells were not considered independent biological replicates.

Exploratory single-cell profiling of cardiac CD45+ cells highlights prominent age-associated transcriptional remodeling in macrophages

To define age-associated immune alterations in the heart, we performed single-cell RNA sequencing on sorted CD45+ cells from young and aged mouse hearts, generating one pooled young and one pooled aged scRNA-seq library. After quality control (Supplementary Fig. 1), a total of 11,711 high-quality CD45+ cells were retained, including 4,201 cells from the young pooled library and 7,510 cells from the aged pooled library. These cells were jointly integrated for exploratory single-cell analysis; sample origins are shown in Supplementary Figure 2. Data integration, clustering and UMAP visualization were performed with Seurat [27]. Eight major clusters were identified on the basis of canonical marker expression and highly variable genes: macrophages, monocytes, dendritic cells (DCs), B cells, T cells, neutrophils, proliferating macrophages, and an "others" cluster (Fig. 2A-B, Supplementary Table 1). Although all clusters were present in both age groups, macrophages comprised the largest fraction of CD45+ cells, accounting for 69.7% of cells in the young pooled library and 78.5% in the aged pooled library, whereas the relative representation of the other immune populations showed more modest differences (Fig. 2B–C).

Canonical markers confirmed cluster identities (Fig. 2D). Exploratory cell-level differential expression analysis of macrophages from aged versus young hearts identified 459 upregulated and 925 downregulated genes (Fig. 2E, Supplementary Table 2); within this dataset, macrophages showed a larger number of differentially expressed genes than the other immune-cell populations examined (Figure 2F). To further compare age-associated transcriptional remodeling across immune populations, we calculated an FC score based on the top age-regulated genes in each subset. Macrophages showed the highest FC score (Fig. 2G) and greater SASP-related transcriptional activity [28] in the aged group (Fig. 2H). These exploratory single-cell analyses highlighted prominent age-associated transcriptional remodeling within the cardiac macrophage compartment, motivating focused analysis of macrophage subpopulations.

Aging reshapes cardiac macrophage composition and reveals an aging-enriched TLF+CD209hi macrophage state

Given the high abundance of macrophages, their pronounced age-associated transcriptional remodeling, and their established role in diastolic dysfunction and cardiac remodeling [4, 29], we next characterized cardiac macrophage heterogeneity in greater detail. Using a curated cardiac macrophage gene signature, cells were classified into previously described subpopulations [5, 29] (Fig. 3A). Four major macrophage subsets were identified. The most abundant were TLF+CD209lo macrophages, characterized by high expression of tissue-resident markers *Timd4*, *Lyve1* and *Folr2* with low *Cd209* expression. A closely related TLF+CD209hi subset expressed similarly high levels of *Timd4*, *Lyve1* and *Folr2* but showed markedly elevated *Cd209a*, *Cd209b*, *Cd209d*, *Cd209f*, *Cd209g*. In addition, MHC-II+ macrophages expressed high levels of antigen-presentation genes (*H2-Aa*, *H2-Eb1*), whereas IFN+ macrophages were defined by interferon-stimulated genes such as *Ifit3* and *Irf7*. Canonical marker expression supported the identity of each subset (Fig. 3C, Supplementary Fig. 3, Supplementary Table 3). While TLF+CD209lo, MHC-II+, and IFN+ macrophages were detected in both age groups, the TLF+CD209hi subset was predominantly detected in the aged group. An alternative Harmony-based integration and reclustering analysis recovered the same four major macrophage states, with similar age-associated distributions and defining marker-expression patterns (Supplementary Fig.19). The relative composition of macrophage subsets differed between the young and aged groups: TLF+ macrophages represented a larger proportion in the aged group, accompanied by enrichment of the TLF+CD209hi population, whereas MHC-II+ macrophages were relatively less represented (Fig. 3B).

To validate these findings at the protein and population levels, we performed flow cytometric analysis, which confirmed age-associated differences in macrophage subset frequencies and enrichment of the TLF+CD209hi population in aged hearts (Fig. 3D; gating strategy shown in Supplementary Fig. 4). Further analysis using broader cellular denominators showed a similar pattern, with reduced frequencies of TLF+CD209lo and MHC-II+ macrophages and an increased frequency of TLF+CD209hi macrophages among total live cells in aged hearts. TLF+CD209hi cells also constituted a greater proportion of the total macrophage compartment with aging (Supplementary Fig. 13). To complement these relative measurements, we additionally quantified macrophage subset abundance as absolute cell numbers normalized to heart tissue weight. The number of TLF+CD209hi macrophages per mg tissue was markedly increased in aged hearts, whereas the absolute numbers of TLF+CD209lo and MHC-II+ macrophages were reduced (Supplementary Fig.14). Together, these independent flow-cytometric measurements support age-associated remodeling of the cardiac macrophage compartment and selective enrichment of the TLF+CD209hi state in aged hearts.

To further validate the resident-macrophage phenotype, we assessed FOLR2 and TIM-4 expression by

flow cytometry (Supplementary Fig. 16–17). Both FOLR2⁺ and TIM-4⁺ macrophages were increased in aged hearts, providing additional protein-level support for age-associated remodeling of the tissue-resident macrophage compartment.

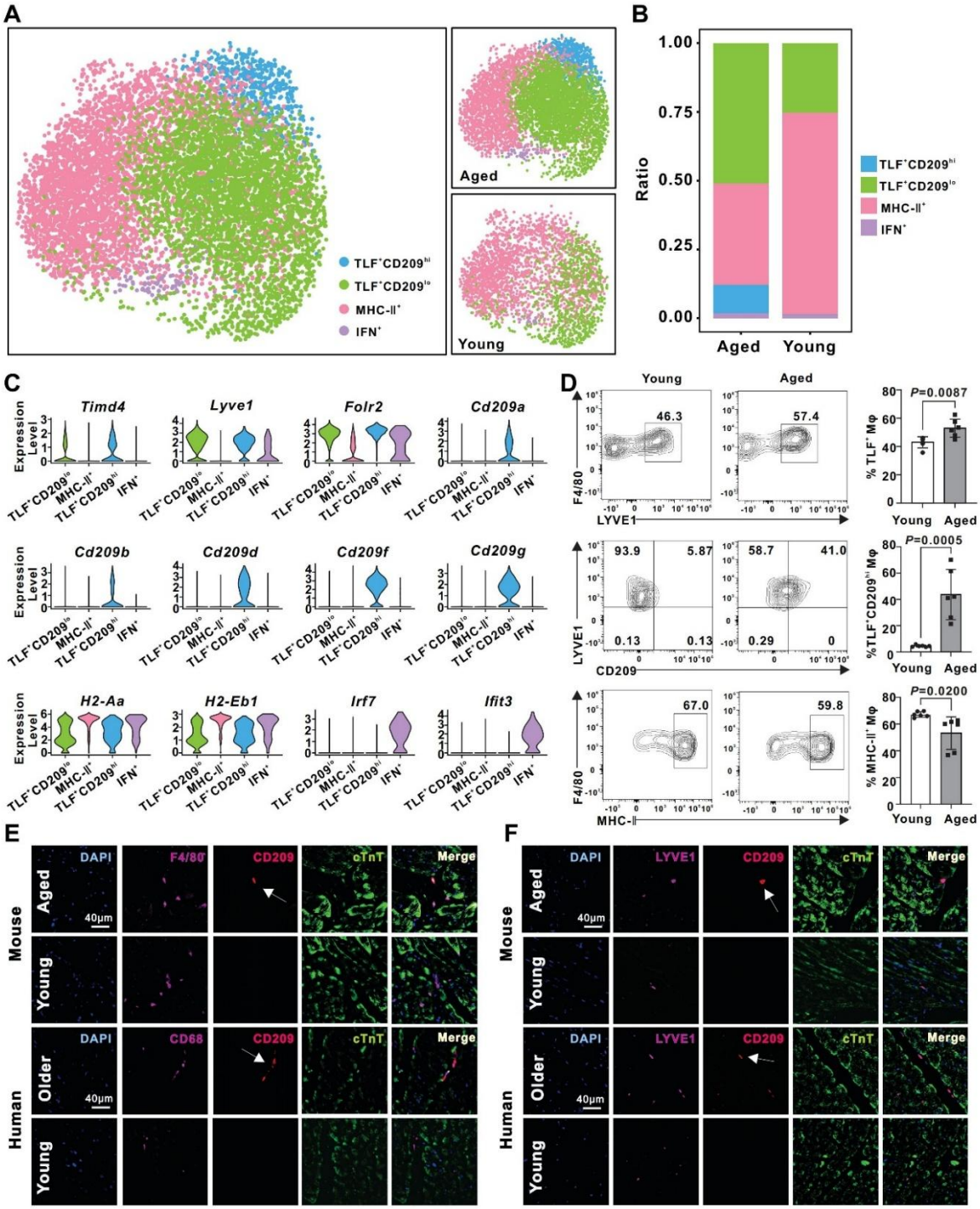


Figure 3. Aging reshapes cardiac macrophage composition and reveals an aging-enriched TLF⁺CD209ʰⁱ macrophage state. (A) UMAP visualization of cardiac macrophages. Left panel shows integrated macrophages from both young and aged groups, colored by subset identity. Right panels show macrophages from young or aged hearts separately. **(B)** Bar plot showing proportion of each macrophage subset in the pooled young and aged scRNA-seq libraries. **(C)** Violin plots showing expression distributions of key marker genes defining each macrophage subset. **(D)** Flow cytometric quantification of macrophage subset frequencies in young and aged hearts (n = 6 mice per group). Representative gating strategy is shown in Supplemental Figure 4. Data are mean ± SEM; *P* values were determined by unpaired two-tailed Student's *t*-test. **(E)** Immunofluorescence staining

showing CD209 expression on cardiac macrophages. Co-staining for pan-macrophage markers (human: CD68; mouse: F4/80; purple), CD209 (red), and cardiomyocytes (cTnT; green) demonstrates marked enrichment of $CD209^+$ macrophages (arrowheads) in aged hearts. **(F)** Immunofluorescence staining for the tissue-resident macrophage marker LYVE1 (purple), CD209 (red), and cardiomyocytes (cTnT; green), showing CD209 localization to $LYVE1^+$ macrophages in aged hearts. Representative images in panels E and F were obtained from young and aged mice (n = 4 per age group) and young and older human donors (n = 4 per age group). Scale bars, as indicated.

Immunofluorescence staining further localized CD209 expression to cardiac macrophages, where it co-localized with the tissue-resident macrophage marker LYVE1 and pan-macrophage markers (F4/80 in mouse hearts and CD68 in human hearts). Notably, $CD209^+$ macrophages were rare or barely detectable in young hearts but readily observed in aged mouse and older human myocardium. (Fig. 3E–F). Together, these data support selective macrophage compositional remodeling with age and enrichment of a TLF^+CD209^{hi} tissue-resident macrophage state in aged hearts.

Aging-associated macrophage remodeling involves senescence-related, pro-inflammatory and profibrotic transcriptional programs

To characterize senescence- and inflammation-related transcriptional patterns in cardiac macrophages, we quantified SASP activity across cardiac macrophages. Aged macrophages showed a pronounced rightward shift in SASP scores [28] relative to young macrophages (Fig. 4A), consistent with greater SASP-related transcriptional activity in the aged group. This finding was also supported by gene-set enrichment analysis comparing aged and young macrophages, which showed enrichment of SASP-related gene sets in aged cells (Supplementary Fig. 5). Consistent with these global changes, module activity scores for the cellular senescence gene set (GO:0090398) showed higher score distributions in aged TLF^+CD209^{lo}, TLF^+CD209^{hi}, and $MHC\text{-}II^+$ macrophage subsets than in their young counterparts (Fig. 4B). In contrast, the IFN^+ macrophage subset showed relatively little difference in senescence-related scores between the two age groups, indicating that senescence-related transcriptional remodeling appeared more pronounced in specific macrophage populations rather than uniformly distributed across all subsets.

To explore state transitions associated with macrophage aging, we reconstructed macrophage trajectories with Slingshot and conducted integrated pseudotemporal analysis (Fig. 4C–D). TradeSeq analysis identified genes with age-associated expression dynamics along pseudotime, which clustered into four major transcriptional modules (C1–C4) (Fig. 4D, Supplementary Table 4). Pathway enrichment collectively indicated age-associated remodeling of inflammatory, fibrosis-related, metabolic-stress, and innate immune programs. These findings further supported coordinated inflammatory and fibrosis-associated transcriptional remodeling of cardiac macrophages with aging.

Density plot analysis showed that macrophages from aged hearts preferentially occupied later pseudotime states compared with those from young hearts (Fig. 4E). Subtype-resolved density plots showed distinct pseudotime distributions, with TLF^+CD209^{hi} macrophages predominantly occupying later pseudotime states in the aged group (Supplementary Fig. 12). PlotSmoother visualization illustrated the dynamic expression of key genes along this trajectory (Fig. 4F): *Cdkn2a* and *Lmna* (senescence markers) [30, 31] were elevated in aged macrophages, accompanied by increased expression of canonical SASP/inflammatory effectors (*Il1b, Il6,* and *Tnf*) [32]. Elevated *Il10* expression suggested concurrent compensatory anti-inflammatory signaling that could paradoxically contribute to profibrotic remodeling [4]. Moreover, upregulation of *Areg* and *Ecm1*, genes implicated in tissue remodeling and extracellular matrix interactions [33, 34], supports a role for aged macrophages in modulating fibroblast activity, particularly at later pseudotime stages (Fig. 4F).

Flow cytometry confirmed enhanced inflammatory cytokine expression in aged cardiac macrophages. Compared with young hearts, aged hearts displayed increased frequencies of $TNF\text{-}\alpha^+$, $IL\text{-}1\beta^+$, and $IL\text{-}6^+$ macrophages, together with elevated cytokine mean fluorescence intensity (MFI) (Fig. 4G-I, Supplementary Fig. 6). Similar increases in both cytokine-positive cell frequencies and MFI were also observed in $MHC\text{-}II^+$ and TLF^+ macrophage subclusters (Supplementary Fig. 6-7). Collectively, these exploratory single-cell analyses, together with flow-cytometric validation of inflammatory cytokine production, support aging-associated reprogramming of cardiac macrophages—particularly TLF^+ and $MHC\text{-}II^+$ subsets—toward senescence-related, pro-inflammatory and profibrotic transcriptional states, implicating macrophage senescence-associated remodeling as a prominent feature of cardiac immune aging.

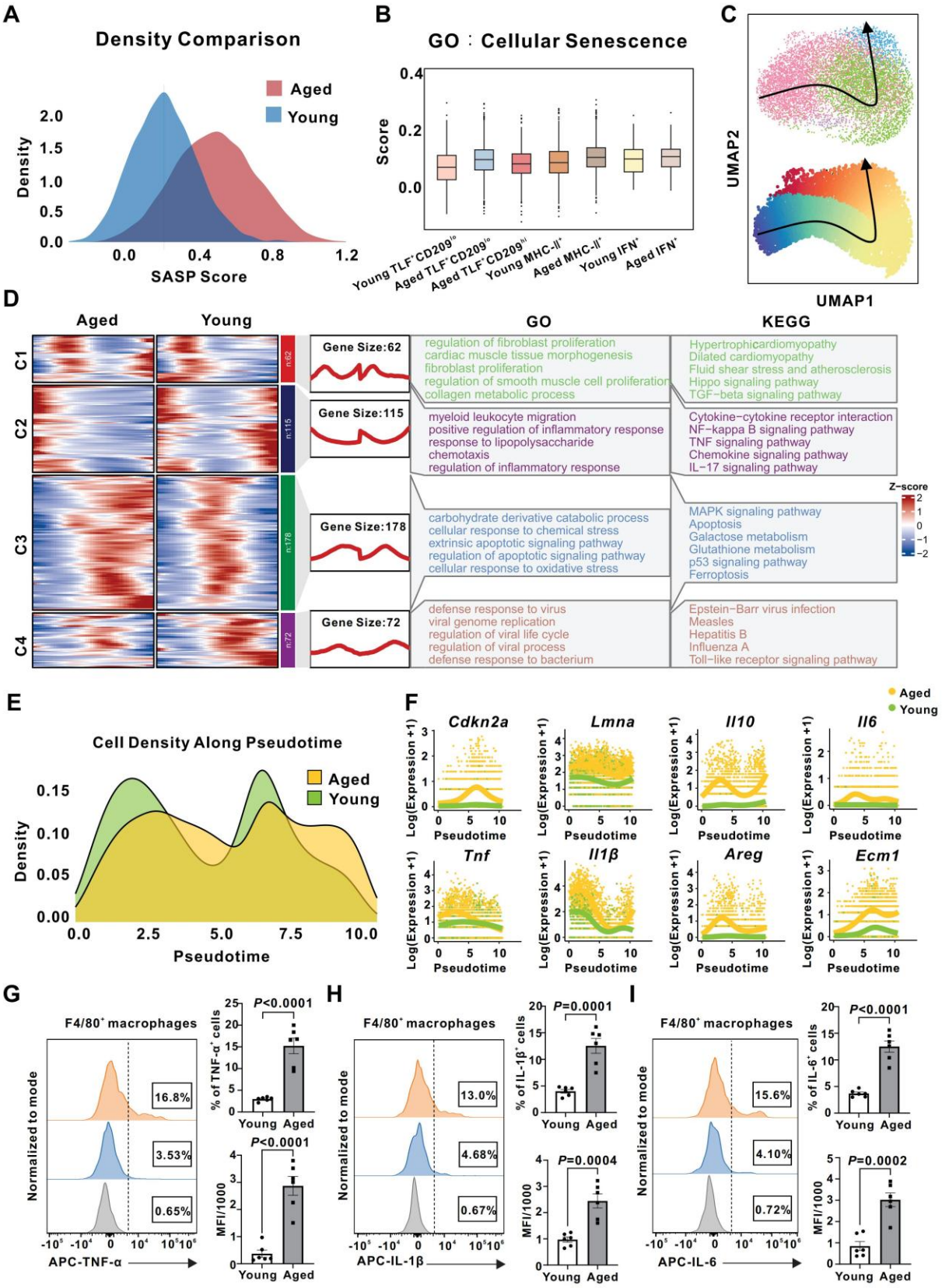

A
Density Comparison
Aged
Young
Density
SASP Score
B
GO：Cellular Senescence
Score
Young TLF+CD209lo
Aged TLF+CD209lo
Aged TLF+CD209hi
Young MHC-II+
Aged MHC-II+
Young IFN+
Aged IFN+
C
UMAP2
UMAP1
D
Aged
Young
GO
KEGG
C1
C2
C3
C4
Gene Size:62
Gene Size:115
Gene Size:178
Gene Size:72
regulation of fibroblast proliferation
cardiac muscle tissue morphogenesis
fibroblast proliferation
regulation of smooth muscle cell proliferation
collagen metabolic process
Hypertrophicardiomyopathy
Dilated cardiomyopathy
Fluid shear stress and atherosclerosis
Hippo signaling pathway
TGF-beta signaling pathway
myeloid leukocyte migration
positive regulation of inflammatory response
response to lipopolysaccharide
chemotaxis
regulation of inflammatory response
Cytokine-cytokine receptor interaction
NF-kappa B signaling pathway
TNF signaling pathway
Chemokine signaling pathway
IL-17 signaling pathway
carbohydrate derivative catabolic process
cellular response to chemical stress
extrinsic apoptotic signaling pathway
regulation of apoptotic signaling pathway
cellular response to oxidative stress
MAPK signaling pathway
Apoptosis
Galactose metabolism
Glutathione metabolism
p53 signaling pathway
Ferroptosis
defense response to virus
viral genome replication
regulation of viral life cycle
regulation of viral process
defense response to bacterium
Epstein-Barr virus infection
Measles
Hepatitis B
Influenza A
Toll-like receptor signaling pathway
Z-score
E
Cell Density Along Pseudotime
Aged
Young
Density
Pseudotime
F
Aged
Young
Cdkn2a
Lmna
Il10
Il6
Tnf
Il1β
Areg
Ecm1
Log(Expression +1)
Pseudotime
G
F4/80+ macrophages
Normalized to mode
16.8%
3.53%
0.65%
APC-TNF-α
% of TNF-α+ cells
P<0.0001
MFI/1000
P<0.0001
Young
Aged
H
F4/80+ macrophages
13.0%
4.68%
0.67%
APC-IL-1β
% of IL-1β+ cells
P=0.0001
MFI/1000
P=0.0004
I
F4/80+ macrophages
15.6%
4.10%
0.72%
APC-IL-6
% of IL-6+ cells
P<0.0001
MFI/1000
P=0.0002

Figure 4. Aging is associated with senescence-related, pro-inflammatory, and fibrosis-associated transcriptional states in cardiac macrophages. (A) Density plots comparing SASP gene-set activity scores (calculated using the AddModuleScore algorithm) in total cardiac macrophages from young and aged hearts. The gene set used here is identical to that employed in Figure 2H**. (B)** Module activity scores for cellular senescence (GO:0090398) were calculated using the AddModuleScore algorithm. Box plots show the median and interquartile range (IQR), with whiskers extending to the most extreme observations within 1.5 × IQR. **(C)** Slingshot-based pseudotime trajectory inference of cardiac macrophages visualized on UMAP coordinates, with inferred lineage and pseudotime progression indicated. **(D)** Integrated pseudotemporal analysis of age-dependent macrophage reprogramming. *Left*: heatmap of genes differentially expressed along pseudotime between young and aged macrophages, grouped into four modules (C1–C4). *Middle*: smoothed mean expression trajectories of each module along pseudotime. *Right*: GO and KEGG pathway enrichment analyses for each module. **(E)** Density plots showing the distribution of young and aged macrophages along the inferred pseudotime trajectory. **(F)** PlotSmoother visualization illustrating the dynamic expression of key senescence-, inflammatory-, and remodeling-associated genes along the pseudotime trajectory. Expression values are presented on a log1p-transformed normalized scale, and smoothed curves represent fitted values from negative binomial generalized additive models (GAMs) using tradeSeq (fitGAM, nknots = 6). **(G-I)** Representative normalized histograms and quantification of inflammatory cytokine expression in cardiac macrophages from young and aged mouse hearts. TNF-α expression is shown in **(G)**, IL-1β expression in **(H)**, and IL-6 expression in **(I).** Numbers in the histograms indicate the percentage of cytokine-positive cells. Bar graphs show quantification of cytokine-positive cell frequency and mean fluorescence intensity (MFI/1000). MFI/1000 indicates the mean fluorescence intensity divided by 1,000. Data are presented as mean ± SEM (n=6 mice per group). *P* values were determined by unpaired two-tailed Student's *t*-test.

Aged cardiac macrophage subpopulations exhibit inflammatory, metabolic, and fibrotic transcriptional remodeling

To delineate how inflammatory and fibrotic programs diverge among cardiac macrophage subsets during aging, we focused on TLF$^+$ and MHC-II$^+$ macrophages and interrogated their underlying regulatory architecture. Exploratory SCENIC [35] suggested subset-specific regulatory remodeling with aging (Fig. 5A). Aged MHC-II$^+$ macrophages showed increased activity of inflammatory regulons, most prominently Nfkb1 and Stat4. Macrophage functional polarization toward a pro-inflammatory phenotype is closely linked to metabolic reprogramming [36], and aged MHC-II$^+$ macrophages accordingly exhibited transcriptional features consistent with reduced oxidative metabolism and increased glycolysis. In contrast, aged TLF$^+$ macrophages exhibited increased activity of fibrosis-associated regulators, including Irf4, Mafb, and Smad1. Notably, Barx2 activity was selectively enriched in aged TLF$^+$CD209^{hi} macrophages, consistent with enhanced cell–matrix and extracellular matrix-associated transcriptional programs [37, 38].

These regulatory distinctions were further supported by PROGENy [39] gene-set enrichment, and metabolic pathway analyses (Fig. 5B–G). Aged MHC-II$^+$ macrophages showed stronger TNF/NF-κB inflammatory activity together with a relative shift from TCA cycle and fatty acid metabolism toward glycolysis, whereas TLF$^+$ macrophages preferentially exhibited fibrosis-associated programs. Together, these analyses suggested functional divergence between an inflammatory MHC-II$^+$ state and a fibrosis-associated TLF$^+$ resident macrophage state during cardiac aging.

Finally, flow cytometric validation confirmed that aged MHC-II$^+$ macrophages represent the dominant source of inflammatory cytokines in the aging heart (Fig. 5H-J, Supplementary Fig. 8). Intracellular cytokine staining revealed that TNF-α$^+$, IL-1β$^+$, and IL-6$^+$ macrophages were predominantly derived from the MHC-II$^+$ rather than TLF$^+$ subset, identifying aged MHC-II$^+$ macrophages as principal inflammatory effectors during cardiac aging.

Aged macrophages exhibit subset-specific EGF-family–EGFR and IL-10-associated PDGF-A/PDGFRα signaling programs

Having observed fibrosis-related transcriptional programs in aged macrophages, particularly within TLF$^+$ populations, we next investigated candidate molecular programs and intercellular signaling networks associated with fibrotic remodeling in the aging heart. GO enrichment analysis showed that TLF$^+$CD209^{lo} macrophages in young hearts were transcriptionally oriented toward tissue homeostasis, with enrichment for pathways linked to environmental surveillance and self-renewal (Fig. 6A). With aging, this population shifted toward a chronically activated state, gaining inflammatory and fibrosis-associated programs including IL-1β production, wound healing, and fibroblast migration. In contrast, aged TLF$^+$CD209^{hi} macrophages displayed a distinct phenotype characterized by metabolic activation and enrichment of tissue-remodeling and angiogenesis pathways (Fig. 6B). Although these features can reflect reparative intent, they were accompanied by fibrosis-related and fibroblast-interacting transcriptional signatures. Direct comparison with aged MHC-II$^+$ macrophages emphasized this divergence: TLF$^+$CD209^{hi} cells were enriched for collagen metabolic processes, fibroblast proliferation and OXPHOS-related programs, whereas MHC-II$^+$ macrophages predominantly exhibited inflammatory signatures (Fig. 6C).

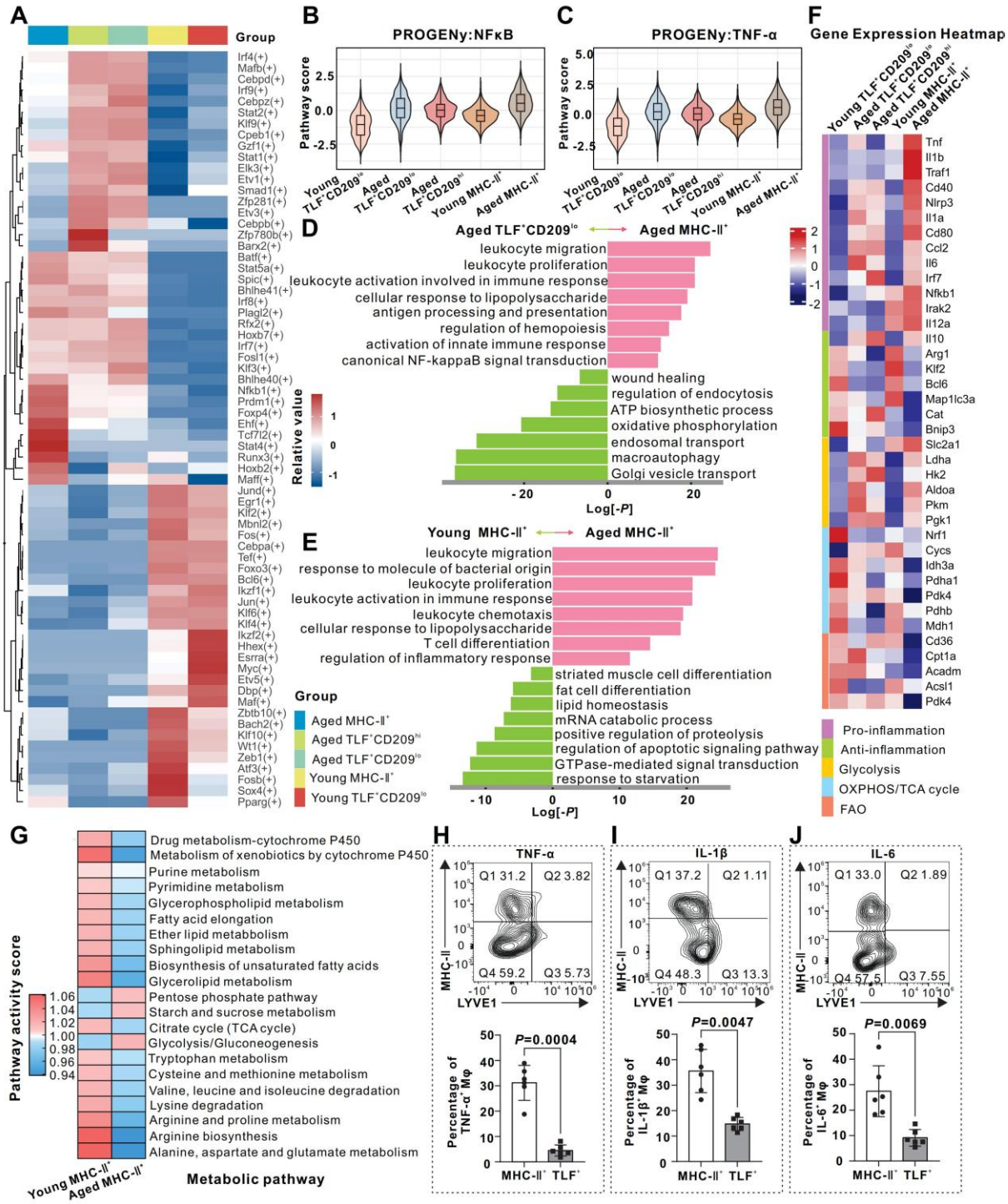


Figure 5. Aging induces inflammatory, metabolic, and fibrotic transcriptional reprogramming of cardiac macrophage subsets. **(A)** Heatmap of inferred transcription factor activity (SCENIC) across cardiac macrophage subsets from young and aged hearts. **(B, C)** Violin plots showing PROGENy pathway activity scores for NF-κB **(B)** and TNF-α **(C)** signaling across macrophage subsets. **(D, E)** Gene-set enrichment analyses comparing aged MHC-II$^+$ versus aged TLF$^+$CD209^{lo} macrophages **(D)** and aged versus young MHC-II$^+$ macrophages **(E)**. Differentially expressed genes were identified using MAST as implemented in Seurat. **(F)** Heatmap of a curated panel of inflammatory and metabolic genes across macrophage subsets. **(G)** Heatmap showing metabolic pathway activity scores inferred from KEGG pathways, highlighting age-associated metabolic reprogramming across macrophage subsets. **(H-J)** Flow cytometric validation of cytokine-producing macrophage subset distribution in aged hearts. Representative contour plots and quantification show the percentages of TNF-α$^+$ **(H)**, IL-1β$^+$ **(I)** and IL-6$^+$ **(J)** macrophages assigned to MHC-II$^+$ or TLF$^+$ subsets. Data are presented as mean ± SEM (n=6 mice per group). *P* values were determined by paired two-tailed Student's *t*-test.

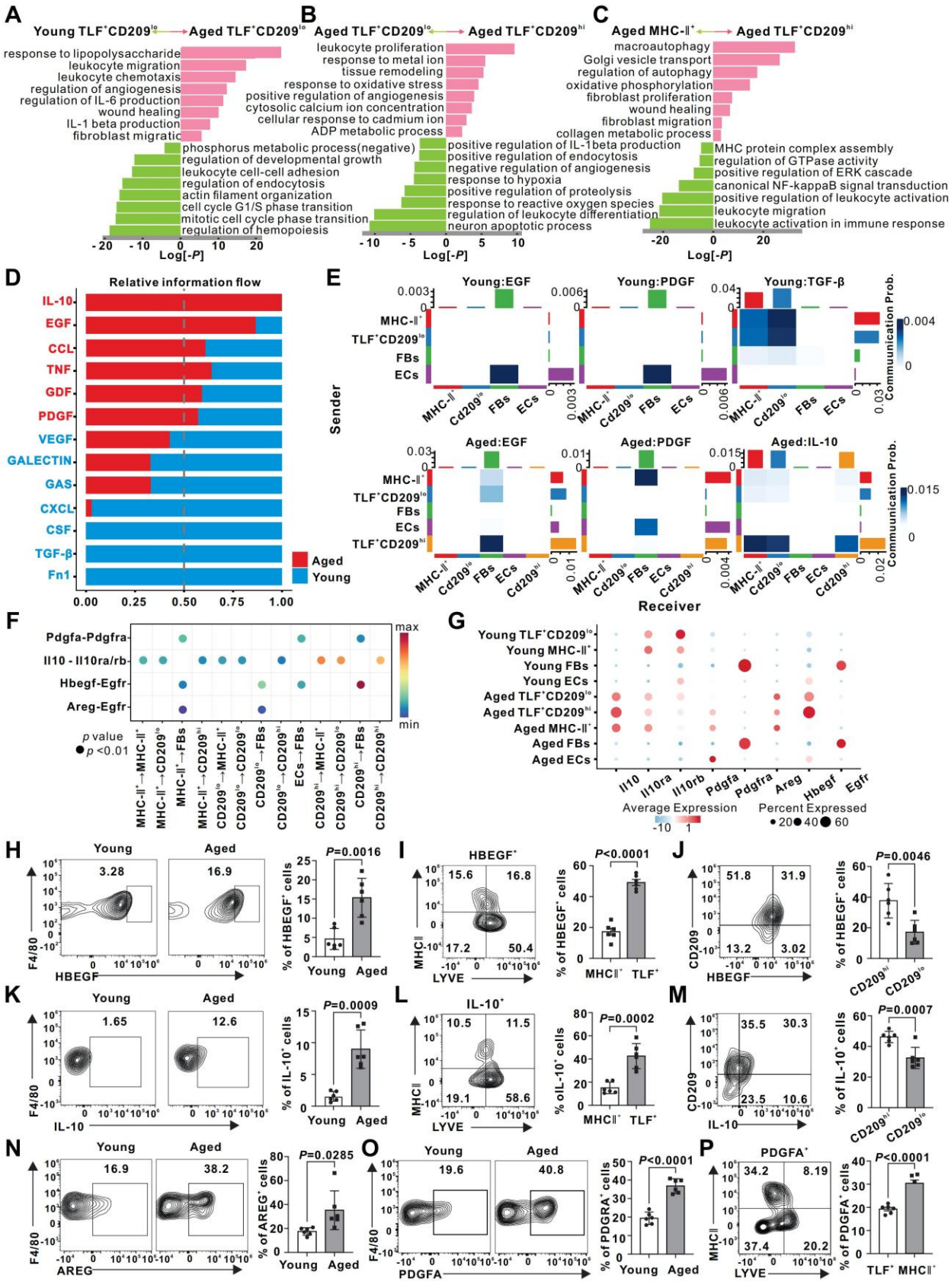

A
Young TLF+CD209lo → Aged TLF+CD209lo
response to lipopolysaccharide
leukocyte migration
leukocyte chemotaxis
regulation of angiogenesis
regulation of IL-6 production
wound healing
IL-1 beta production
fibroblast migratic
phosphorus metabolic process(negative)
regulation of developmental growth
leukocyte cell-cell adhesion
regulation of endocytosis
actin filament organization
cell cycle G1/S phase transition
mitotic cell cycle phase transition
regulation of hemopoiesis
Log[-P]
B
Aged TLF+CD209lo → Aged TLF+CD209hi
leukocyte proliferation
response to metal ion
tissue remodeling
response to oxidative stress
positive regulation of angiogenesis
cytosolic calcium ion concentration
cellular response to cadmium ion
ADP metabolic process
positive regulation of IL-1beta production
positive regulation of endocytosis
negative regulation of angiogenesis
response to hypoxia
positive regulation of proteolysis
response to reactive oxygen species
regulation of leukocyte differentiation
neuron apoptotic process
Log[-P]
C
Aged MHC-II+ → Aged TLF+CD209hi
macroautophagy
Golgi vesicle transport
regulation of autophagy
oxidative phosphorylation
fibroblast proliferation
wound healing
fibroblast migration
collagen metabolic process
MHC protein complex assembly
regulation of GTPase activity
positive regulation of ERK cascade
canonical NF-kappaB signal transduction
positive regulation of leukocyte activation
leukocyte migration
leukocyte activation in immune response
Log[-P]
D
Relative information flow
IL-10
EGF
CCL
TNF
GDF
PDGF
VEGF
GALECTIN
GAS
CXCL
CSF
TGF-β
Fn1
Aged
Young
E
Young:EGF
Young:PDGF
Young:TGF-β
Aged:EGF
Aged:PDGF
Aged:IL-10
Sender
Receiver
Communication Prob.
MHC-II+
TLF+CD209lo
FBs
ECs
TLF+CD209hi
F
Pdgfa-Pdgfra
Il10 - Il10ra/rb
Hbegf-Egfr
Areg-Egfr
max
min
p value
p <0.01
G
Young TLF+CD209lo
Young MHC-II+
Young FBs
Young ECs
Aged TLF+CD209lo
Aged TLF+CD209hi
Aged MHC-II+
Aged FBs
Aged ECs
Il10
Il10ra
Il10rb
Pdgfa
Pdgfra
Areg
Hbegf
Egfr
Average Expression
Percent Expressed
H
Young
Aged
3.28
16.9
F4/80
HBEGF
P=0.0016
% of HBEGF+ cells
I
HBEGF+
15.6
16.8
17.2
50.4
MHCII
LYVE
P<0.0001
% of HBEGF+ cells
MHCII+
TLF+
J
51.8
31.9
13.2
3.02
CD209
HBEGF
P=0.0046
% of HBEGF+ cells
CD209hi
CD209lo
K
Young
Aged
1.65
12.6
F4/80
IL-10
P=0.0009
% of IL-10+ cells
L
IL-10+
10.5
11.5
19.1
58.6
MHCII
LYVE
P=0.0002
% of IL-10+ cells
M
35.5
30.3
23.5
10.6
CD209
IL-10
P=0.0007
% of IL-10+ cells
N
Young
Aged
16.9
38.2
F4/80
AREG
P=0.0285
% of AREG+ cells
O
Young
Aged
19.6
40.8
F4/80
PDGFA
P<0.0001
% of PDGRA+ cells
P
PDGFA+
34.2
8.19
37.4
20.2
MHCII
LYVE
P<0.0001
% of PDGFA+ cells
TLF+
MHCII+

Figure 6. Aged macrophages exhibit subset-specific candidate profibrotic signaling programs involving EGF-family–EGFR and IL-10-associated PDGF-A/PDGFRα axes. (A–C) GO enrichment analyses of differentially expressed genes across macrophage subclusters: aged versus young TLF$^+$CD209^{lo} macrophages **(A)**, aged TLF$^+$CD209^{hi} versus aged TLF$^+$CD209^{lo} **(B)**, and aged TLF$^+$CD209^{hi} versus aged MHC-II$^+$ macrophages **(C)**. Differentially expressed genes were identified using MAST as implemented in Seurat. **(D)** Relative information-flow analysis inferred by CellChat, summarizing the contribution of major signaling pathways in young and aged hearts. **(E)** CellChat netVisual heatmaps showing interaction strengths between sender and receiver cell populations for selected signaling pathways. FBs, fibroblasts; ECs, endothelial cells. **(F)** Bubble plots showing selected predicted ligand–receptor interactions involving EGF-family/EGFR, IL-10/IL-10R and PDGF-A/PDGFRα signaling in aged hearts. Dot size represents statistical significance and color reflects communication probability. **(G)** Dot plot showing average expression levels and fractions of expressing cells for key genes in EGF-family and IL-10–PDGFA pathways across macrophage subsets. **(H–P)** Flow cytometric analysis of HB-EGF, IL-10, AREG, and PDGF-A expression in cardiac macrophages. **(H, K, N, O)** Representative plots and quantification of HB-EGF$^+$, IL-10$^+$, AREG$^+$, and PDGF-A$^+$ cells among F4/80$^+$ macrophages from young and aged hearts. **(I, L, P)** Distribution of HB-EGF$^+$, IL-10$^+$, and PDGF-A$^+$ macrophages between MHC-II$^+$ and TLF$^+$ subsets in aged hearts. **(J, M)** Frequencies of HB-EGF$^+$ and IL-10$^+$ cells within TLF$^+$CD209^{hi} and TLF$^+$CD209^{lo} aged macrophages. Numbers in plots indicate gated cell percentages. Data are presented as mean ± SEM (n = 6 mice per group). *P* values were determined using unpaired two-tailed Student's t-tests for comparisons between young and aged groups and paired two-tailed Student's t-tests for macrophage subset comparisons.

Analysis of extracellular matrix–related GO terms across macrophages revealed age-associated differences in fibrosis-related transcriptional programs (Supplementary Fig. 9A). Epidermal growth factor (EGF) receptor signaling emerged as the most strongly enriched pathway in aged macrophages, together with enhanced TNF signaling, while canonical TGF-β signaling was relatively downregulated. Notably, IL-10 and platelet-derived growth factor (PDGF) receptor signaling were also enriched. Prior work showing IL-10–dependent induction of PDGF-A in macrophages and its role in fibroblast activation provides a mechanistic precedent for these non-canonical profibrotic circuits in aging tissue [40, 41].

Consistent with these pathway-level findings, fibrosis-related gene expression changed markedly with age (Supplementary Fig. 9B). Young macrophages preferentially expressed TGF-β pathway components (for example, *Tgfb1*, *Acta2*, *Fn1*, *Spp1*) and anti-fibrotic regulator *Pten* [42], whereas aged macrophages—especially TLF$^+$CD209^{hi} cells—upregulated EGF-family ligands, IL-10 and a suite of extracellular matrix genes, supporting a prominent profibrotic transcriptional signature in this subset.

CellChat analysis [26] of a comprehensive dataset encompassing fibroblasts, endothelial, and immune cells (Supplementary Fig. 10) predicted age-associated changes in intercellular communication (Fig. 6D-E). CellChat inferred higher relative communication activity for EGF, IL-10, and PDGF signaling in aged hearts, whereas TGF-β signaling was predicted to be more prominent in young hearts. In young hearts, EGF signaling was largely endothelial→ fibroblast; whereas in aged hearts, TLF$^+$CD209^{hi} macrophages were predicted to represent a major source of EGF-family signals targeting fibroblasts (Fig. 6G). IL-10 signaling was predicted in aged hearts but was not detected by CellChat in young hearts, with TLF$^+$CD209^{hi} macrophages predicted as major senders to other macrophage subsets. PDGF signaling similarly shifted from endothelial→fibroblast in young hearts to macrophage→fibroblast in aged hearts, with fibroblasts as the major predicted recipient population (Fig. 6D-E).

Ligand–receptor analysis [26] identified *Hbegf–Egfr* as a prominent candidate macrophage→fibroblast interaction in aged hearts (Fig. 6F), with *Hbegf* expression largely confined to TLF$^+$CD209^{hi} macrophages and *Egfr* expression enriched in fibroblasts (Fig. 6G). Amphiregulin (*Areg*)–*Egfr* was also predicted as a candidate interaction within this signaling axis. Concurrently, *Il10* expression was higher in aged TLF$^+$CD209^{hi} macrophages, *Il10ra/Il10rb* and *Pdgfa* were enriched in aged macrophages, and *Pdgfra* expression was restricted to fibroblasts (Fig. 6G). Correlation and interaction analyses supported a putative *Il10*-associated (macrophage→macrophage) *Pdgfa* (macrophage→fibroblast) signaling relationship with potential relevance to fibroblast activation and proliferation (Fig. 6F, Supplementary Fig. 9C-D).

Flow cytometric validation confirmed increased protein expression of HB-EGF, AREG, PDGF-A and IL-10 in aged macrophages compared with young controls (Fig. 6H, K, N, O). Subset analysis showed that HB-EGF$^+$ and IL-10$^+$ macrophages were preferentially enriched in the TLF$^+$ compartment, whereas PDGF-A$^+$ macrophages were predominantly enriched within the MHC-II$^+$ subset (Fig. 6I, L, P). Within aged TLF$^+$ macrophages, CD209^{hi} cells showed higher frequencies of HB-EGF$^+$ and IL-10$^+$ cells than their CD209^{lo} counterparts (Fig. 6J, M; Supplementary Fig. 11).

Together, the exploratory transcriptomic analyses and independent flow-cytometric validation support subset-specific profibrotic mediator profiles in aged cardiac macrophages, linking TLF$^+$CD209^{hi} macrophages to HB-EGF/AREG–EGFR and IL-10 signaling and MHC-II$^+$ macrophages to PDGF-A production. These findings nominate a candidate macrophage-associated signaling network that may promote fibroblast activation and

matrix remodeling during cardiac aging.

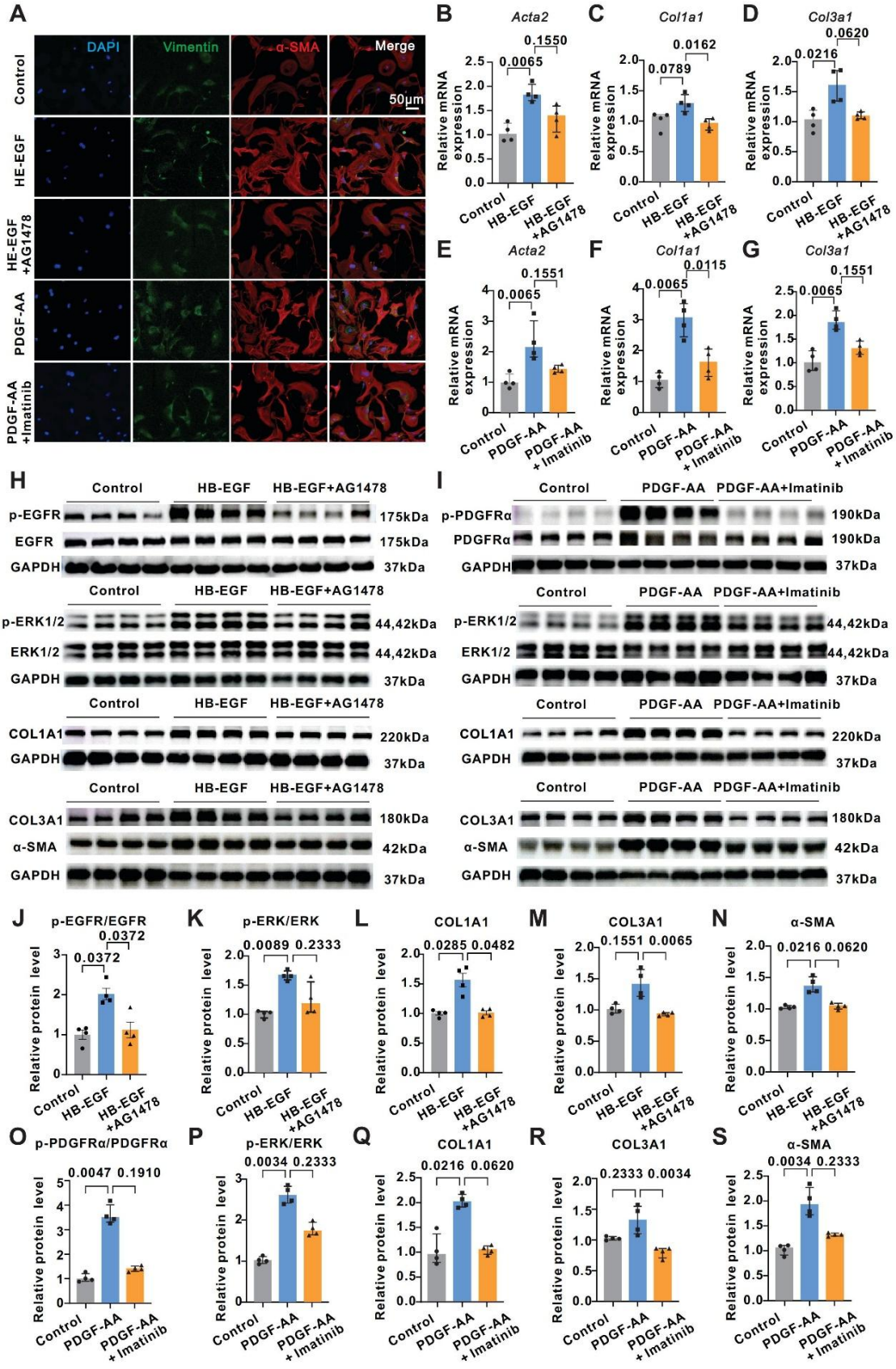


Figure 7. HB-EGF and PDGF-AA are sufficient to activate cardiac fibroblasts through EGFR/ERK and PDGFRα/ERK signaling. HB-EGF and PDGF-AA were used at 100 ng/mL, with AG1478 (2 μM) or imatinib (1 μM), respectively, administered 60 min before ligand stimulation. Phosphorylation assays (panels H and I) were performed after 15 min of stimulation, RT-qPCR analyses (panels B–G) after 24 h, and immunofluorescence (panel A) and fibrotic protein expression assays (panels H and I) after 48 h. **(A)** Representative immunofluorescence images of primary adult mouse cardiac fibroblasts treated with HB-EGF or PDGF-AA in the presence or absence of AG1478 or imatinib, respectively. Cells were stained for vimentin (green), α-SMA (red), and DAPI (blue). Scale bar, 50 μm. **(B–D)** RT-qPCR analysis of *Acta2* **(B)**, *Col1a1* **(C)**, and *Col3a1* **(D)** expression in control, HB-EGF-treated, and HB-EGF plus AG1478-treated fibroblasts. **(E–G)** RT-qPCR analysis of *Acta2* **(E)**, *Col1a1* **(F)**, and *Col3a1* **(G)** expression in control, PDGF-AA-treated, and PDGF-AA plus imatinib-treated fibroblasts. **(H, I)** Representative immunoblots showing receptor and ERK1/2 phosphorylation and fibrotic marker expression following HB-EGF treatment with or without AG1478 **(H)** or PDGF-AA treatment with or without imatinib **(I)**. Although presented together in panels H and I, the phosphorylation and fibrotic protein-expression blots were obtained from separate experiments at the respective time points described above**. (J–N)** Quantification of p-EGFR/EGFR **(J)**, p-ERK1/2/ERK1/2 **(K)**, COL1A1 **(L)**, COL3A1 **(M)**, and α-SMA **(N)** protein levels in the HB-EGF experiments. **(O–S)** Quantification of p-PDGFRα/PDGFRα **(O)**, p-ERK1/2/ERK1/2 **(P)**, COL1A1 **(Q)**, COL3A1 **(R)**, and α-SMA **(S)** protein levels in the PDGF-AA experiments. Fibrotic protein levels were normalized to GAPDH and expressed relative to the control group. Data are presented as median with interquartile range (n = 4 per group). Statistical significance was assessed using the Kruskal–Wallis test followed by Dunn's multiple-comparisons test for two prespecified pairwise comparisons within each panel. Exact *P* values are shown in the corresponding panels.

Candidate macrophage-associated ligands HB-EGF and PDGF-AA activate cardiac fibroblasts with EGFR/ERK and PDGFRα/ERK signaling

To test whether the candidate ligands were sufficient to directly activate cardiac fibroblasts in the absence of age-associated preconditioning, we examined the effects of HB-EGF and PDGF-AA on primary fibroblasts isolated from young adult mouse hearts. Immunofluorescence staining showed that control cardiac fibroblasts displayed vimentin positivity with relatively limited α-SMA-positive stress fiber organization. In contrast, stimulation with recombinant HB-EGF or PDGF-AA promoted cell spreading and markedly enhanced filamentous α-SMA-positive stress fiber formation, consistent with myofibroblast-like activation. These phenotypic changes were attenuated by pretreatment with the EGFR inhibitor AG1478 or the PDGFR inhibitor imatinib, respectively (Fig. 7A).

RT-qPCR analyses showed that both ligands increased the expression of multiple fibrosis-associated genes, with statistically significant changes in selected markers. AG1478 and imatinib attenuated some of these transcriptional responses, although the inhibitory effects were not consistently significant across all genes (Fig. 7B–G).

Western blot analyses further demonstrated increased phosphorylation of EGFR/ERK and PDGFRα/ERK following HB-EGF and PDGF-AA treatment, respectively, accompanied by increased expression of selected fibrotic proteins. Pharmacological inhibition significantly reduced certain readouts, but did not consistently suppress all measured signaling and fibrotic markers (Fig. 7H–S).

Together, these findings support the ability of HB-EGF and PDGF-AA to promote cardiac fibroblast activation in vitro and suggest involvement of their corresponding receptor-associated signaling pathways, while the variable inhibitor responses limit definitive conclusions regarding pathway dependence.

DISCUSSION

In this study, we identify an aging-enriched TLF⁺CD209^{hi} macrophage state within the tissue-resident macrophage compartment, characterized by a distinct fibrosis-associated signaling program. Aging is accompanied by diastolic dysfunction, ventricular remodeling, and increased myocardial fibrosis in mice—hallmarks of cardiac aging that predispose to HFpEF [43]. These structural and functional changes were paralleled by expansion and transcriptional reprogramming of cardiac macrophages. Exploratory single-cell transcriptomic profiling highlighted macrophages as a prominently remodeled immune population in the aging heart, consistent with prior studies demonstrating age-associated changes in cardiac macrophage abundance and phenotype and implicating macrophages in cardiac fibrosis and diastolic dysfunction [3, 4, 44]. Aged macrophages exhibited increased SASP transcriptional activity, increased pro-inflammatory cytokine expression, and coordinated pro-fibrotic programs. Integration of transcriptional regulatory network analysis, cell–cell communication inference, and protein-level validation identified an HB-EGF/AREG–EGFR axis and an IL-10-associated PDGF-A/PDGFRα signaling as candidate mechanisms linking aged macrophages to fibroblast activation. Collectively, these findings highlight aging-associated macrophage reprogramming and macrophage–fibroblast communication as prominent features and candidate contributors to myocardial fibrotic remodeling.

Our results extend prior work on cardiac macrophage heterogeneity by showing that aging is associated not only with changes in macrophage abundance and activation state, but also with enrichment of a distinct CD209^{hi}

transcriptional and phenotypic state within the tissue-resident macrophage compartment. Fate-mapping and single-cell studies have established the existence of long-lived TIMD4^{+}/LYVE1^{+}/FOLR2^{+} resident macrophages and functionally distinct CCR2^{+}/MHC-II^{hi} recruited populations in the heart [5]. Importantly, our data do not establish TLF^{+}CD209^{hi} macrophages as a distinct developmental lineage. Rather, their shared expression of *Timd4*, *Lyve1*, and *Folr2* supports their interpretation as an age-associated CD209^{hi} state within the established TLF^{+} resident macrophage compartment. This state was transcriptionally linked to extracellular matrix remodeling and fibroblast-interacting signaling programs, with functional support from ligand-sufficiency assays showing that candidate macrophage-associated ligands can activate cardiac fibroblasts. This observation helps reconcile the dual roles of cardiac macrophages in tissue homeostasis versus pathological remodeling depending on subset identity and context [5, 45]. Importantly, whereas most prior studies have focused on macrophage responses to acute injury such as myocardial infarction, our data suggest that physiological aging is accompanied by macrophage specialization toward fibrosis-associated signaling states.

Mechanistically, our data suggest a model in which three complementary features of aged macrophages may collectively shape a fibroblast-interacting profibrotic milieu. First, senescence-related transcriptional remodeling and increased SASP-related activity may contribute to sustained macrophage paracrine signaling, including IL-1β, IL-6, TNF-α and growth factors, which are known to modulate fibroblast activation and extracellular matrix turnover [46]. Senescent immune cells have been increasingly recognized as contributors to inflammaging and age-related fibrotic disease across organs [30, 46]. Second, metabolic reprogramming—characterized by enhanced glycolytic programs in inflammatory MHC-II^{+} macrophages and relative preservation of oxidative metabolism in profibrotic resident macrophage states—provides the bioenergetic context shaping macrophage effector function, consistent with established links between metabolism and macrophage polarization [47]. Third, the ligand–receptor architecture identified here (HB-EGF/AREG→EGFR and an IL-10-linked PDGF-A/PDGFRα signaling axis) provides molecular routes by which macrophages may influence fibroblast proliferation and collagen production. Crucially, our *in vitro* functional assays, utilizing HB-EGF as a representative EGF-family ligand together with PDGF-AA, provide functional evidence that these candidate ligands can activate fibroblast signaling. HB-EGF and PDGF-AA induced receptor-associated ERK1/2 phosphorylation and increased selected fibrosis-associated markers, supporting their ability to promote fibroblast activation in vitro. Although AG1478 and imatinib attenuated some of these responses, the effects were not consistently significant across all measured outcomes, indicating that the contribution of these signaling pathways requires further investigation. These findings are consistent with and extend prior evidence that EGFR ligands, including AREG and HB-EGF, participate in fibrotic remodeling in the lung, liver, and heart [48-50], as well as recent evidence that IL-10 can program macrophages toward PDGF-A expression and profibrotic activity in tissue repair and fibrosis models [40].

These mechanistic insights suggest several therapeutic opportunities. Targeting macrophage senescence using senolytics or SASP modulators has shown efficacy in reducing age-related tissue dysfunction in preclinical models [30, 51]. Reprogramming macrophage metabolism or interrupting macrophage–fibroblast signaling through inhibition of EGFR or PDGFR pathways represents another strategy, although systemic blockade of these pathways is limited by on-target toxicity [52, 53]. In this context, macrophage-targeted delivery approaches or ligand-specific neutralization may offer more favorable therapeutic windows. Importantly, aging-associated myocardial fibrosis and immune dysregulation are central features of HFpEF, a syndrome in which cardiomyocyte-directed therapies have largely failed [43, 54]. The detection of increased CD209^{+} macrophages in older human myocardium provides supportive cross-species evidence for the translational relevance of macrophage-centric mechanisms in human cardiac aging.

Conclusions

In conclusion, our integrated multi-modal analysis identifies an aging-enriched TLF^{+}CD209^{hi} macrophage state within the tissue-resident macrophage compartment, associated with coordinated senescence-, metabolism-, and signaling-related programs. These findings nominate HB-EGF/AREG–EGFR and IL-10-associated PDGF-A/PDGFRα signaling axes as candidate contributors to fibroblast activation, myocardial fibrosis, and diastolic dysfunction during cardiac aging. Their causal roles in vivo, however, remain to be established through targeted genetic or pharmacologic perturbation. Together, these findings highlight macrophage remodeling and macrophage–fibroblast communication as candidate mechanisms for further investigation in cardiac aging.

Limitations

Although this study provides insights into candidate macrophage–fibroblast signaling interactions during cardiac aging, several limitations should be

acknowledged. First, the scRNA-seq analysis was based on one pooled young library and one pooled aged library. Therefore, individual cells should not be considered independent biological replicates, and age-associated transcriptomic and compositional differences should be interpreted primarily as exploratory findings. Independent biological replication will be required to confirm these observations. Second, although integrated transcriptomic analysis, ligand–receptor inference, protein-level validation, and ligand-stimulation assays support an association between $TLF^{+}CD209^{hi}$ macrophages and candidate HB-EGF/AREG–EGFR and IL-10-associated PDGF-A/PDGFRα profibrotic signaling axes, definitive causality will require macrophage- or fibroblast-specific genetic and pharmacologic perturbation in aging models. Third, fibroblasts from young adult mice were deliberately used to assess the effects of HB-EGF and PDGF-AA in the absence of age-associated preconditioning. Whether fibroblasts from aged hearts exhibit comparable responses to these ligands remains to be determined. Fourth, all mouse experiments were performed exclusively in male mice. Given the well-established sex differences in cardiac aging and myocardial remodeling, whether the age-associated macrophage states and candidate macrophage–fibroblast signaling pathways identified here are similarly present in females remains to be determined. Future studies incorporating both sexes will be required to determine the sex dependence and generalizability of these findings. Fifth, although physiological cardiac aging shares important pathological features with HFpEF, including diastolic dysfunction and myocardial fibrosis, it does not fully recapitulate the clinical heterogeneity of the syndrome. Finally, human data were limited to immunostaining of post-mortem myocardial tissue and therefore provide supportive but not cell-resolved validation; spatial transcriptomics, single-cell profiling, or larger clinically annotated cohorts of aged human hearts will be important future steps.

Ethics approval and consent to participate

Human post-mortem myocardial tissue use was approved by the Ethics Committee of Tongji Medical College, Huazhong University of Science and Technology (No. IROG20250841), with written informed consent obtained from next of kin. All animal procedures were approved by the Institutional Animal Care and Use Committee of Tongji Medical College, Huazhong University of Science and Technology (No. 20240305684).

Conflict of Interest

None declared.

Funding

This work was supported by the National Natural Science Foundation of China (Grant Number 82271621, 82672076) and the Interdisciplinary Research Program of HUST (Grant Number 2025JCYJ076).

Author Contribution

C.F and K.L: conception and design of the study. YZ.Q and XY.M: experiments and data acquisition. L.R and ZL.L: human sample preparation. Y.S, TH.A and ZH.W: data analysis. XX.H and ZY.W: animal work.

Acknowledgement

We thank the Department of Forensic Medicine, Tongji Medical College, Huazhong University of Science and Technology, for assistance with the collection and processing of human cardiac tissue samples. We are grateful to members of the laboratory for helpful discussions and technical assistance throughout the study.

Data Availability Statement

All data supporting the findings of this study are available within the article, its supplemental materials, and the Zenodo repository (https://zenodo.org/records/24053768). The single-cell RNA-sequencing data generated in this study have been deposited in the NCBI Gene Expression Omnibus (GEO) under accession number GSE351491. The complete analysis code used for the single-cell RNA-sequencing and downstream computational analyses in this study is publicly available in a separate Zenodo repository (https://doi.org/10.5281/zenodo.23301758).

Supplementary Materials

The Supplementary data can be found online at: www.aginganddisease.org/EN/10.14336/AD.2026.1022.

References

[1] Ye M, Feng S, Xu Z, He W, Liu C, Zhu W (2026). Aging and metabolism in HFpEF: Pathophysiology and therapeutic implications. Metabolism, 176:156460.

[2] Lafuse WP, Wozniak DJ, Rajaram MVS (2021). Role of Cardiac Macrophages on Cardiac Inflammation, Fibrosis and Tissue Repair. Cells, 10:51.

[3] Li J, Xin Y, Wang Z, Li J, Li W, Li H (2023). The role of cardiac resident macrophage in cardiac aging. Aging Cell, 22:e14008.

[4] Hulsmans M, Sager HB, Roh JD, Valero-Muñoz M, Houstis NE, Iwamoto Y, et al. (2018). Cardiac

macrophages promote diastolic dysfunction. J Exp Med, 215:423-440.
[5] Dick SA, Macklin JA, Nejat S, Momen A, Clemente-Casares X, Althagafi MG, et al. (2019). Self-renewing resident cardiac macrophages limit adverse remodeling following myocardial infarction. Nat Immunol, 20:29-39.
[6] Dick SA, Wong A, Hamidzada H, Nejat S, Nechanitzky R, Vohra S, et al. (2022). Three tissue resident macrophage subsets coexist across organs with conserved origins and life cycles. Sci Immunol, 7:eabf7777.
[7] Xiao J, Li HS, Satyanarayanan SK, Leung SL, Yuan Q, Wang Y, et al. (2025). Advancements in Targeting Macrophage Senescence for Age-Associated Conditions. Aging Dis, 16:2201-2236.
[8] Campbell RA, Docherty MH, Ferenbach DA, Mylonas KJ (2021). The Role of Ageing and Parenchymal Senescence on Macrophage Function and Fibrosis. Front Immunol, 12:700790.
[9] Pérez S, Rius-Pérez S (2022). Macrophage Polarization and Reprogramming in Acute Inflammation: A Redox Perspective. Antioxidants, 11:1394.
[10] Zhang L, Han H, Xu A, Sathe A, Fu S, Zhao J, et al. (2024). Lysozyme 1 Inflamed CCR2+ Macrophages Promote Obesity-Induced Cardiac Dysfunction. Circ Res, 135:596-613.
[11] Gong S, Zhai M, Shi J, Yu G, Lei Z, Shi Y, et al. (2024). TREM2 macrophage promotes cardiac repair in myocardial infarction by reprogramming metabolism via SLC25A53. Cell Death Differ, 31:239-253.
[12] Pinto AR, Ilinykh A, Ivey MJ, Kuwabara JT, D'Antoni ML, Debuque R, et al. (2016). Revisiting Cardiac Cellular Composition. Circ Res, 118:400-9.
[13] Zhang C, Wang X, Feng C, Zheng H, Leng S, Jiang Y, et al. (2025). Avian GCGR-mediated continuous fat utilization offers perspectives for obesity treatment. Nat Commun, 16:11706.
[14] Chen S, Zhou Y, Chen Y, Gu J (2018). fastp: an ultra-fast all-in-one FASTQ preprocessor. Bioinformatics, 34:i884-i890.
[15] Liao Y, Smyth GK, Shi W (2014). featureCounts: an efficient general purpose program for assigning sequence reads to genomic features. Bioinformatics, 30:923-930.
[16] Lun ATL, Riesenfeld S, Andrews T, Dao TP, Gomes T, Marioni JC (2019). EmptyDrops: distinguishing cells from empty droplets in droplet-based single-cell RNA sequencing data. Genome Biol, 20:63.
[17] Butler A, Hoffman P, Smibert P, Papalexi E, Satija R (2018). Integrating single-cell transcriptomic data across different conditions, technologies, and species. Nat Biotechnol, 36:411-420.
[18] Germain PL, Lun A, Garcia Meixide C, Macnair W, Robinson MD (2021). Doublet identification in single-cell sequencing data using scDblFinder. F1000Res, 10:979.
[19] Yang S, Corbett SE, Koga Y, Wang Z, Johnson WE, Yajima M, et al. (2020). Decontamination of ambient RNA in single-cell RNA-seq with DecontX. Genome Biol, 21:57.
[20] Korsunsky I, Millard N, Fan J, Slowikowski K, Zhang F, Wei K, et al. (2019). Fast, sensitive and accurate integration of single-cell data with Harmony. Nat Methods, 16:1289-1296.
[21] Finak G, McDavid A, Yajima M, Deng J, Gersuk V, Shalek AK, et al. (2015). MAST: a flexible statistical framework for assessing transcriptional changes and characterizing heterogeneity in single-cell RNA sequencing data. Genome Biol, 16:278.
[22] Hu Y, Wang Y, Zhi L, Yu L, Hu X, Shen Y, et al. (2024). SDC4 protein action and related key genes in nonhealing diabetic foot ulcers based on bioinformatics analysis and machine learning. Int J Biol Macromol, 283:137789.
[23] Street K, Risso D, Fletcher RB, Das D, Ngai J, Yosef N, et al. (2018). Slingshot: cell lineage and pseudotime inference for single-cell transcriptomics. BMC Genomics, 19:477.
[24] Van den Berge K, Roux de Bézieux H, Street K, Saelens W, Cannoodt R, Saeys Y, et al. (2020). Trajectory-based differential expression analysis for single-cell sequencing data. Nat Commun, 11:1201.
[25] Xiao Z, Dai Z, Locasale JW (2019). Metabolic landscape of the tumor microenvironment at single cell resolution. Nat Commun, 10:3763.
[26] Jin S, Guerrero-Juarez CF, Zhang L, Chang I, Ramos R, Kuan CH, et al. (2021). Inference and analysis of cell-cell communication using CellChat. Nat Commun, 12:1088.
[27] Stuart T, Butler A, Hoffman P, Hafemeister C, Papalexi E, Mauck WM, 3rd, et al. (2019). Comprehensive Integration of Single-Cell Data. Cell, 177:1888-1902.e21.
[28] Suryadevara V, Hudgins AD, Rajesh A, Pappalardo A, Karpova A, Dey AK, et al. (2024). SenNet recommendations for detecting senescent cells in different tissues. Nat Rev Mol Cell Biol, 25:1001-1023.
[29] Panico C, Felicetta A, Kunderfranco P, Cremonesi M, Salvarani N, Carullo P, et al. (2024). Single-Cell RNA Sequencing Reveals Metabolic Stress-Dependent Activation of Cardiac Macrophages in a Model of Dyslipidemia-Induced Diastolic Dysfunction. Circulation, 150:1517-1532.
[30] Baker DJ, Wijshake T, Tchkonia T, LeBrasseur NK, Childs BG, van de Sluis B, et al. (2011). Clearance of p16Ink4a-positive senescent cells delays ageing-associated disorders. Nature, 479:232-6.
[31] Cenni V, Capanni C, Mattioli E, Schena E, Squarzoni S, Bacalini MG, et al. (2020). Lamin A involvement in ageing processes. Ageing Res Rev, 62:101073.
[32] Wang B, Han J, Elisseeff JH, Demaria M (2024). The senescence-associated secretory phenotype and its physiological and pathological implications. Nat Rev Mol Cell Biol, 25:958-978.
[33] Wang MH, Liu J, Li SL, Zheng MZ, Qu RY, Xiang M (2025). Amphiregulin: a potential therapeutic target for tissue fibrosis. Trends Pharmacol Sci, 46:877-890.
[34] Hardy SA, Liesinger L, Patrick R, Poettler M, Rech L, Gindlhuber J, et al. (2023). Extracellular Matrix Protein-1 as a Mediator of Inflammation-Induced Fibrosis After

Myocardial Infarction. JACC Basic Transl Sci, 8:1539-1554.
[35] Aibar S, González-Blas CB, Moerman T, Huynh-Thu VA, Imrichova H, Hulselmans G, et al. (2017). SCENIC: single-cell regulatory network inference and clustering. Nat Methods, 14:1083-1086.
[36] O'Neill LA, Pearce EJ (2016). Immunometabolism governs dendritic cell and macrophage function. J Exp Med, 213:15-23.
[37] Meech R, Edelman DB, Jones FS, Makarenkova HP (2005). The homeobox transcription factor Barx2 regulates chondrogenesis during limb development. Development, 132:2135-46.
[38] Tsau C, Ito M, Gromova A, Hoffman MP, Meech R, Makarenkova HP (2011). Barx2 and Fgf10 regulate ocular glands branching morphogenesis by controlling extracellular matrix remodeling. Development, 138:3307-17.
[39] Schubert M, Klinger B, Klünemann M, Sieber A, Uhlitz F, Sauer S, et al. (2018). Perturbation-response genes reveal signaling footprints in cancer gene expression. Nat Commun, 9:20.
[40] Bhattacharyya A, Boostanpour K, Bouzidi M, Magee L, Chen TY, Wolters R, et al. (2022). IL10 trains macrophage profibrotic function after lung injury. Am J Physiol Lung Cell Mol Physiol, 322:L495-L502.
[41] Gallini R, Lindblom P, Bondjers C, Betsholtz C, Andrae J (2016). PDGF-A and PDGF-B induces cardiac fibrosis in transgenic mice. Exp Cell Res, 349:282-290.
[42] Parapuram SK, Shi-wen X, Elliott C, Welch ID, Jones H, Baron M, et al. (2011). Loss of PTEN expression by dermal fibroblasts causes skin fibrosis. J Invest Dermatol, 131:1996-2003.
[43] Sharma K, Kass DA (2014). Heart Failure With Preserved Ejection Fraction. Circ Res, 115:79-96.
[44] Esfahani NS, Wu Q, Kumar N, Ganesan LP, Lafuse WP, Rajaram MVS (2021). Aging influences the cardiac macrophage phenotype and function during steady state and during inflammation. Aging Cell, 20:e13438.
[45] Frantz S, Nahrendorf M (2014). Cardiac macrophages and their role in ischaemic heart disease. Cardiovasc Res, 102:240-8.
[46] Müller L, Di Benedetto S (2025). Immunosenescence and inflammaging: Mechanisms and modulation through diet and lifestyle. Front Immunol, 16:1708280.
[47] Yarbro JR, Emmons RS, Pence BD (2020). Macrophage Immunometabolism and Inflammaging: Roles of Mitochondrial Dysfunction, Cellular Senescence, CD38, and NAD. Immunometabolism, 2:e200026.
[48] Zaiss DMW, Gause WC, Osborne LC, Artis D (2015). Emerging functions of amphiregulin in orchestrating immunity, inflammation, and tissue repair. Immunity, 42:216-226.
[49] Lian H, Ma Y, Feng J, Dong W, Yang Q, Lu D, et al. (2012). Heparin-binding EGF-like growth factor induces heart interstitial fibrosis via an Akt/mTor/p70s6k pathway. PLoS One, 7:e44946.
[50] Fujino T, Hasebe N, Fujita M, Takeuchi K, Kawabe J, Tobise K, et al. (1998). Enhanced expression of heparin-binding EGF-like growth factor and its receptor in hypertrophied left ventricle of spontaneously hypertensive rats. Cardiovasc Res, 38:365-74.
[51] Kirkland JL, Tchkonia T, Zhu Y, Niedernhofer LJ, Robbins PD (2017). The Clinical Potential of Senolytic Drugs. J Am Geriatr Soc, 65:2297-2301.
[52] Tallquist M, Kazlauskas A (2004). PDGF signaling in cells and mice. Cytokine Growth Factor Rev, 15:205-13.
[53] Force T, Kolaja KL (2011). Cardiotoxicity of kinase inhibitors: the prediction and translation of preclinical models to clinical outcomes. Nat Rev Drug Discov, 10:111-126.
[54] Mishra S, Kass DA (2021). Cellular and molecular pathobiology of heart failure with preserved ejection fraction. Nat Rev Cardiol, 18:400-423.